J Adv Ceram

Research Article

Nature-inspired (Ti,Zr,Hf)C/SiC micro-nano composites with enhanced ablation resistance through a Gobi Desert-like protective oxide layer

Li Lu[1], Shuibin Wang[1], Tianxing Jiang[1], Pengcheng Du[2], Jinrun Hu[1], Tianci Zhou[1], Yichen Wang[1,✉], Yi Zeng[1], Yalei Wang[1], Xiang Xiong[1], Qingbo Wen[1]

Cite this article: Lu L, Wang S, Jiang T, et al. *J Adv Ceram* 2025, **14**(10): 9221151. https://doi.org/10.26599/JAC.2025.9221151

ABSTRACT: (Ti,Zr,Hf)C/SiC composites with micro-nano structure were designed inspired by the gravel–sand structure of the wind-resistant Gobi Desert to prevent air-plasma flame scouring and obtain excellent ablation resistance. Dense (Ti,Zr,Hf)C/SiC micro-nano composites were synthesized via pyrolysis of $Ti_{0.2}$–$Zr_{0.3}$–$Hf_{0.5}$–vinylhydridopolycarbosilane (VHPCS) precursors with different contents of $(Ti_{0.33}Zr_{0.33}Hf_{0.34})C$ micropowders and sintered at 2200 °C. During heat treatment, the elemental diffusion between micropowders and polymer-derived ceramics leads to the formation of a single-phase $(Ti_{0.32}Zr_{0.32}Hf_{0.36})C$ solid solution with both micro- and nano-grains. Compared with the micro composites, micro-nano composites exhibit enhanced ablation resistance at approximately 2200 °C, with negative linear and mass ablation rates of −0.12 μm/s and −1.01 mg/s, respectively. This improvement results from the formation of a stable and dense protective oxide layer consisting of microscale $(Ti,Zr,Hf)O_2$ skeletons derived from $(Ti_{0.32}Zr_{0.32}Hf_{0.36})C_{micro}$, uniformly dispersed $(Ti,Zr,Hf)O_2$ nanoparticles derived from $(Ti_{0.32}Zr_{0.32}Hf_{0.36})C_{nano}$, and a SiO_2/$(Zr,Hf)TiO_4$ phase matrix. The refractory $(Ti,Zr,Hf)O_2$ microskeletons and nanoparticles collectively protect the molten matrix from air-plasma flame scouring, similar to the wind-resistant mechanism of the Gobi Desert, in which multisized gravel stabilizes the mobile sands.

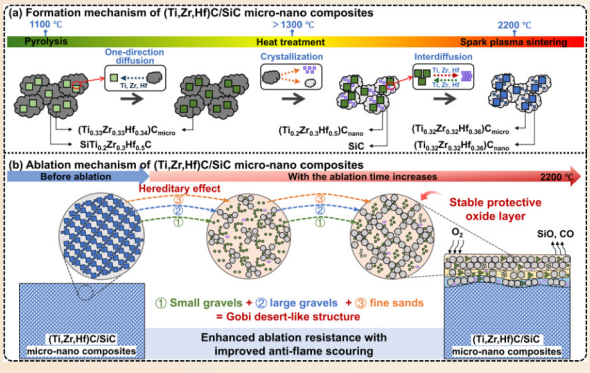

KEYWORDS: ultrahigh-temperature ceramics (UHTCs); micro-nano composites; polymer-derived ceramics (PDCs); nature-inspired; ablation resistance

1 Introduction

In recent years, rapid advancements in aerospace technology have increased the demand for improved thermal protection materials (TPMs). Typical TPMs include refractory metals [1], carbon fiber-reinforced ceramic matrix composites [2–5], and ultrahigh-temperature ceramics (UHTCs) [6,7]. TPMs used in high-speed vehicle components (nose cones or leading edges) must withstand ultrahigh-temperature oxidation and scouring introduced by high-speed airflow. Therefore, their oxidation resistance and structural stability of the oxide layers during ablation are highly important. UHTCs and their composites have emerged as formidable contenders for TPMs [8–11], and their properties are closely related to their chemical composition and microstructure. To improve the ablation resistance of UHTCs and their composites, it is essential to optimize the synthesis methods, chemical composition, and microstructure design.

A series of techniques have been widely used to fabricate UHTCs and their composites, including solid-state reaction (SSR) [12–15], sol–gel method [16,17], polymer-derived ceramic (PDC) [18–20], reactive melt infiltration (RMI) [21,22], chemical vapor deposition (CVD) [23,24], and polymer infiltration and pyrolysis (PIP) [25–27]. Among these methods, the PDC method facilitates effective composition and phase modulation through the precise molecular design of polymer precursors (including the types and ratios of ultrahigh-temperature elements). Furthermore, the UHTC phases are generated *in situ* in/with the SiC matrix, achieving uniform phase dispersion [28]. Lu *et al.* [29] synthesized nanoscale Ta_4HfC_5 ceramics with well-distributed elements via the PDCs method. Yang *et al.* [30] prepared (TiHfVNbTa)C high-entropy carbides from a homogeneous multimetal polymer precursor, with a significant compositional improvement over high-entropy carbides produced via an SSR method. Thus, the PDC method is a promising approach for the preparation of

[1] State Key Laboratory of Powder Metallurgy, Central South University, Changsha 410083, China. [2] Hunan Jinyu Advanced Materials Co., Ltd., Changsha 410200, China.

✉ Corresponding author. E-mail: yichenwang@csu.edu.cn

Received: May 7, 2025; Revised: August 12, 2025; Accepted: August 14, 2025

nanoscale multicomponent UHTCs with tailored phase compositions and uniform microstructures, leading to improved properties.

In previous studies, a series of dense UHTCs/SiC nanocomposites with uniform microstructures and elements, such as HfC/SiC [31], (Hf,Ta)C/SiC [32,33], and (Ti,Zr,Hf)C/SiC [34], were synthesized via the PDC method. These nanocomposites show superior oxidation performance at medium–high temperatures (500–1600 °C) and enhanced ablation resistance at high temperatures (approximately 2200 °C). Among these composites, $(Ti_{0.2}Zr_{0.3}Hf_{0.5})C$/SiC nanocomposites achieved enhanced ablation resistance because of the formation of a dense multi-oxide layer including (Ti,Zr,Hf)O_2, (Zr,Hf)TiO_4, and SiO_2 phases during ablation. The presence of high-melting-point (Ti,Zr,Hf)O_2 nanoparticles significantly enhances the stability of the oxide layer via the pinning effect. The oxide layer thus offers great protection against the invasion of oxygen atoms, as well as good resistance to the air-plasma flame scouring [34,35]. However, the loss of molten phases in the oxide layer of $(Ti_{0.2}Zr_{0.3}Hf_{0.5})C$/SiC nanocomposites can still be observed during ablation, which indicates that the simple (Ti,Zr,Hf)O_2 nanoparticles are unable to sufficiently stabilize the oxide layer.

Enhancing the stability of the oxide layer through microstructure design is a promising new strategy to improve the ablation resistance of (Ti,Zr,Hf)C/SiC composites. Inspired by natural geological systems, desert regions with fine sand are characterized by a high degree of mobility, whereas the Gobi Desert (commonly found in Northwestern China), which comprises multi-sized gravel and fine sand, is characterized by strong wind resistance. The surface gravel layer has been shown to effectively reduce near-surface wind speeds, whereas the underlying sand has been observed to form a compacted matrix within the interstitial spaces of the gravel [36]. This structure allows the Gobi Desert to maintain good stability even under strong windy conditions and offers a nature-inspired microstructure design for enhancing the stability of the oxide layer in anti-ablation materials. This motivated the development of UHTCs-based composites with multiscale Gobi Desert-like structures, such as (Ti,Zr,Hf)C/SiC micro-nano composites, then to preserve the stabilized Gobi Desert-like structure in the oxide layer on the basis of the hereditary effects of the material structure to synergistically improve ablation resistance.

In this work, (Ti,Zr,Hf)C/SiC micro-nano composites and microcomposites with varying (Ti,Zr,Hf)C contents were prepared by combining the PDC and SSR methods. The formation process and mechanism of micro-nano (Ti,Zr,Hf)C composites were investigated. The ablation resistance and underlying mechanisms of micro-nano composites at approximately 2200 °C were discussed and compared with those of microcomposites. The synergistic effect of micro-nano (Ti,Zr,Hf)C grains in enhancing the ablation resistance of composites was demonstrated, highlighting their role in stabilizing protective oxide layers during ablation. This work proposes a simple and new strategy to improve the ablation resistance of UHTCs-based composites through microstructure design.

2 Experimental

2.1 Materials preparation

2.1.1 *Preparation of $(Ti_{0.33}Zr_{0.33}Hf_{0.34})C$ powders*

Commercially available Ti, Zr, Hf, and carbon powders (> 99.5 wt%, 1–3 μm, Macklin Biochemical Co., China) were used as the starting materials for the synthesis of $(Ti_{0.33}Zr_{0.33}Hf_{0.34})C$ through the SSR method. The starting materials were weighed according to the target compositions, i.e., the molar ratio of Ti : Zr : Hf : C was 1 : 1 : 1 : 3. The powders were mixed through high-energy ball milling at 300 r/min for 6 h. Then, the mixed powders were annealed at 2000 °C under an argon atmosphere to obtain a solid solution $(Ti_{0.33}Zr_{0.33}Hf_{0.34})C$ powder. Detailed preparation information is reported elsewhere [13].

2.1.2 *Preparation of micro-nano composites*

A schematic diagram of the preparation of UHTC micro-nano composites is shown in Fig. 1. First, the as-prepared micro-$(Ti_{0.33}Zr_{0.33}Hf_{0.34})C$ powders (4, 8, and 12 g) were mixed with 3 g of vinylhydridopolycarbosilane (VHPCS, Institute of Chemistry, Chinese Academy of Sciences, China) and 5 mL of xylene, forming a $(Ti_{0.33}Zr_{0.33}Hf_{0.34})C_{micro}$/VHPCS slurry mixtures. A solution containing three metal amides (i.e., tetrakis (dimethylamino)titanium(IV) (TDMAT), tetrakis(dimethylamino) zirconium(IV) (TDMAZ), and tetrakis(dimethylamino) hafnium(IV) (TDMAH)) (Nanjing Ai Mou Yuan Scientific

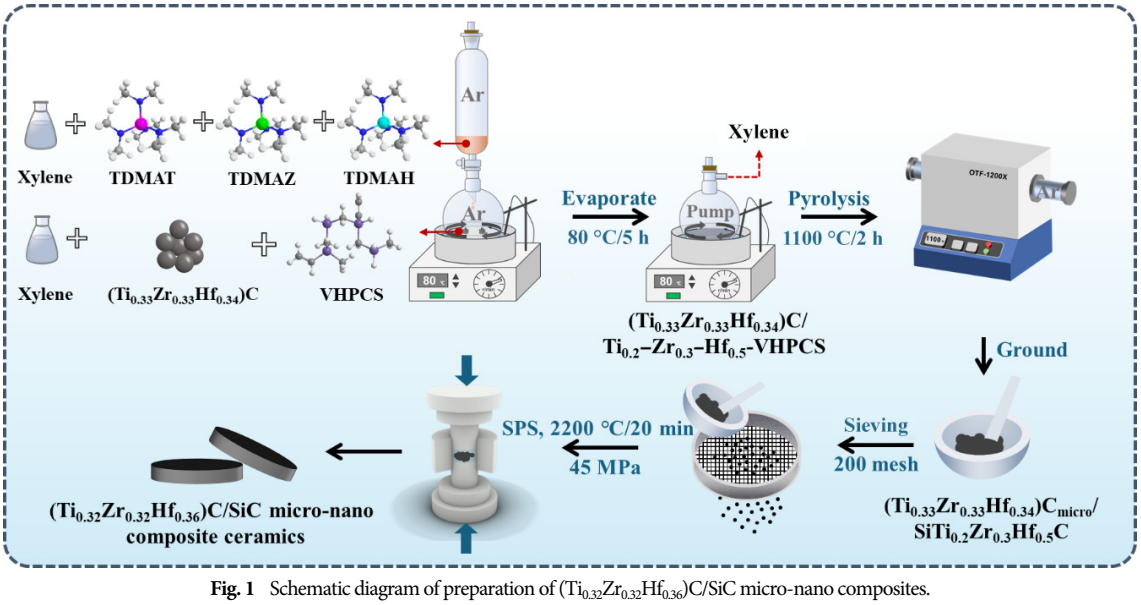

Fig. 1 Schematic diagram of preparation of $(Ti_{0.32}Zr_{0.32}Hf_{0.36})C$/SiC micro-nano composites.

Equipment Co., Ltd., China) (7 g in total) in a molar ratio of 2 : 3 : 5 was subsequently titrated into the $(Ti_{0.33}Zr_{0.33}Hf_{0.34})C_{micro}$/VHPCS mixtures and heated at 80 °C for 3 h with stirring. According to our previous work [34], these three metal amides can react with VHPCS to form a $Ti_{0.2}$–$Zr_{0.3}$–$Hf_{0.5}$–VHPCS single-source precursor (SSP). The whole reaction process was conducted under an argon atmosphere via the Schlenk technique to prevent the hydrolysis of the precursors. Interestingly, because the $Ti_{0.2}$–$Zr_{0.3}$–$Hf_{0.5}$–VHPCS crosslinked during heating and stirring, the $(Ti_{0.33}Zr_{0.33}Hf_{0.34})C$ powders were fixed in the crosslinked $Ti_{0.2}$–$Zr_{0.3}$–$Hf_{0.5}$–VHPCS without sedimentation. After further evaporating the xylene under vacuum at 80 °C for 5 h, a black solid-state mixture with $(Ti_{0.33}Zr_{0.33}Hf_{0.34})C$ powders homogeneously dispersed in the SSP was obtained (denoted as $(Ti_{0.33}Zr_{0.33}Hf_{0.34})C_{micro}$/$Ti_{0.2}$–$Zr_{0.3}$–$Hf_{0.5}$–VHPCS). Then, the as-obtained mixtures were pyrolyzed at 1100 °C for 2 h in argon to obtain $(Ti_{0.33}Zr_{0.33}Hf_{0.34})C_{micro}$/$SiTi_{0.2}Zr_{0.3}Hf_{0.5}C$-based ceramics (according to Ref [34], the ceramic yield of $Ti_{0.2}$–$Zr_{0.3}$–$Hf_{0.5}$–VHPCS was 75 wt% after pyrolysis, and $SiTi_{0.2}Zr_{0.3}Hf_{0.5}C$ indicates an amorphous state). The $(Ti_{0.33}Zr_{0.33}Hf_{0.34})C_{micro}$/$SiTi_{0.2}Zr_{0.3}Hf_{0.5}C$ ceramics are denoted as STZHC-1, STZHC-2, and STZHC-3, respectively, according to the different amounts of added $(Ti_{0.33}Zr_{0.33}Hf_{0.34})C$ powders (4, 8, and 12 g, respectively). The high-temperature phase evolution of the as-pyrolyzed ceramics was studied by annealing at 1300, 1500, and 1600 °C in argon for 5 h. Furthermore, the as-pyrolyzed ceramics were densified via the spark plasma sintering (SPS) process in a furnace (FCT HP D25, FCT Systeme GmbH, Germany) under a pressure of 45 MPa at 2200 °C for 20 min under vacuum. The skeletal density and open porosity of the samples were determined by Archimedes' method with deionized water as the immersion medium.

For comparison, the $(Ti_{0.33}Zr_{0.33}Hf_{0.34})C$ powders were also mixed with the pure VHPCS to prepare dense $(Ti_{0.33}Zr_{0.33}Hf_{0.34})C_{micro}$/SiC micro-composites under the same conditions. To ensure that the content of the UHTCs phases in the $(Ti_{0.33}Zr_{0.33}Hf_{0.34})C_{micro}$/SiC dense composites is the same as that in the sintered STZHC-1, STZHC-2, and STZHC-3 composites, the weights of $(Ti_{0.33}Zr_{0.33}Hf_{0.34})C$ powders in the $(Ti_{0.33}Zr_{0.33}Hf_{0.34})C_{micro}$/VHPCS mixtures were set to 8, 12, and 16 g, respectively (these weights were calculated based on a ceramic yield of 65 wt% for VHPCS). They are denoted as SC-1, SC-2, and SC-3, respectively. The contents of the components before and after the SPS process can be found in Table 1.

2.2 Ablation test

The ablation behavior of the sintered STZHC-1/2/3 and SC-1/2/3 ceramics with dimensions of ϕ20 mm × 4 mm was evaluated using air-plasma equipment for 60 s. The working current and voltage for all tested samples were set at 550 A and 58 V to ensure the same heat flux. The fluxes were 2000 and 150 L/h for argon and hydrogen gas, respectively. The distance between the nozzle and the sample surface was 60 mm, and the surface temperature of each sample was recorded with an infrared thermometer. The mass ablation rate (R_m, mg/s) and linear ablation rate (R_l, μm/s) were calculated using Eqs. (1) and (2):

$$R_m = \frac{\Delta m}{t} = \frac{m_0 - m_1}{t} \quad (1)$$

$$R_l = \frac{\Delta l}{t} = \frac{l_0 - l_1}{t} \quad (2)$$

where m_0 and m_1 are the masses of the samples before and after ablation (mg), respectively; l_0 and l_1 are the thicknesses of the samples before and after ablation (μm), respectively; t is the ablation time (s).

2.3 Characterizations

An X-ray diffractometer (XRD; Smartlab SE, Japan) with Cu Kα1 radiation was used to determine the phase composition of the annealed powders and sintered samples before and after ablation. An inductively coupled plasma-atomic emission spectrometer (ICP-AES; iCap 6500, Thermo Fisher Scientific, USA) was used to analyze the contents of Ti, Zr, and Hf elements in the sintered samples. A scanning electron microscope (SEM; CLARA, TESCAN, The Czech Republic) with an energy dispersive spectrometer (EDS) detector was applied to investigate the morphologies of the composites before and after ablation, as well as their element distribution. A transmission electron microscope (TEM; Talos, F200X, Czech Republic) equipped with an EDS was used to characterize the microstructures of the ceramics.

3 Results and discussion

3.1 Microstructure of $(Ti_{0.33}Zr_{0.33}Hf_{0.34})C$ powders

Figure 2(a) shows the XRD patterns of the as-prepared $(Ti_{0.33}Zr_{0.33}Hf_{0.34})C$ powders, which were annealed at 2000 °C. Only one set of diffraction peaks appears in the annealed powders, which shows that a single-phase solid solution $(Ti_{0.33}Zr_{0.33}Hf_{0.34})C$ formed after high-temperature treatment. As indicated by the XRD refinement results (Fig. 2(b)), the values of the weighted profile residual factor (R_{wp}) and the profile residual factor (R_p) converge to 3.70% and 2.58% for the $(Ti_{0.33}Zr_{0.33}Hf_{0.34})C$, suggesting well fit with experimental results. The lattice constant of $(Ti_{0.33}Zr_{0.33}Hf_{0.34})C$ is 0.4578 nm, which agrees well with the results calculated by Vegard's law [37]. The SEM images and EDS mappings of the $(Ti_{0.33}Zr_{0.33}Hf_{0.34})C$ powder show a uniform distribution of C, Ti, Zr, and Hf elements at the microscale (Fig. 2(c)). The microstructure of the $(Ti_{0.33}Zr_{0.33}Hf_{0.34})C$ powder

Table 1 Composition (weight fractions) before and after SPS process and chemical formula of sintered composites for each sample (different precursors were used to prepare PDCs for two groups of samples: $Ti_{0.2}$–$Zr_{0.3}$–$Hf_{0.5}$–VHPCS used for STZHC samples and VHPCS used for SC samples)

Sample	Before SPS (wt%)		After SPS (wt%)		Chemical formula
	$(Ti_{0.33}Zr_{0.33}Hf_{0.34})C$	PDCs	(Ti,Zr,Hf)C	SiC	
STZHC-1	34.8	65.2	70.7	29.3	$(Ti_{0.32}Zr_{0.32}Hf_{0.36})C/30SiC$
STZHC-2	51.6	48.4	78.2	21.8	$(Ti_{0.32}Zr_{0.32}Hf_{0.36})C/22SiC$
STZHC-3	61.5	38.5	82.7	17.3	$(Ti_{0.32}Zr_{0.32}Hf_{0.36})C/17SiC$
SC-1	60.3	39.7	70.0	30.0	$(Ti_{0.33}Zr_{0.33}Hf_{0.34})C/30SiC$
SC-2	69.7	30.3	78.0	22.0	$(Ti_{0.33}Zr_{0.33}Hf_{0.34})C/22SiC$
SC-3	75.9	24.1	82.9	17.1	$(Ti_{0.33}Zr_{0.33}Hf_{0.34})C/17SiC$

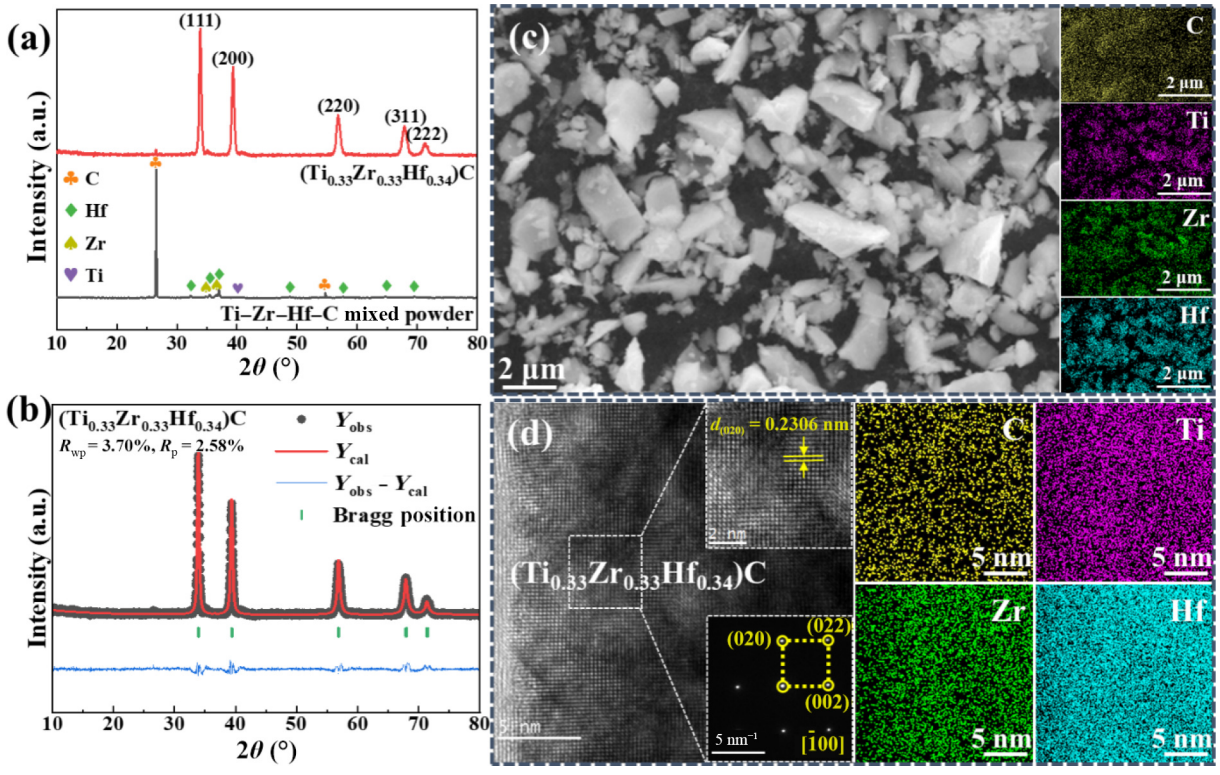

Fig. 2 (a) XRD patterns of Ti, Zr, Hf, and C powder mixtures and annealed $(Ti_{0.33}Zr_{0.33}Hf_{0.34})C$ powder; (b) fitted XRD profile, (c) SEM image, and (d) TEM images of $(Ti_{0.33}Zr_{0.33}Hf_{0.34})C$ single-phase solid solutions.

was also characterized via TEM (Fig. 2(d)), and the lattice spacing of the (020) crystal plane was determined to be 0.2306 nm from high-resolution TEM (HRTEM), which is close to the XRD refinement result. The selected area electron diffraction (SAED) pattern indicates the face-centered cubic (FCC) structure of $(Ti_{0.33}Zr_{0.33}Hf_{0.34})C$ powder as well. In addition, the element distribution mappings of C, Ti, Zr, and Hf further prove the uniformity of the solid solution powder at the nanoscale.

3.2 Microstructure of micro-nano composites and micro composites

XRD patterns and enlarged XRD patterns of the STZHC-1/2/3 micro-nano composites and SC-1/2/3 micro composites are shown in Fig. 3 and Fig. S1 in the Electronic Supplementary Material (ESM). They were pyrolyzed at 1100 °C and subsequently annealed at 1300, 1500, 1600 °C and sintered by SPS technology at 2200 °C. All the as-pyrolyzed powders exhibit a set of well-crystallized diffraction peaks belonging to the previously mixed $(Ti_{0.33}Zr_{0.33}Hf_{0.34})C$ micropowders. Under these conditions, the $SiTi_{0.2}Zr_{0.3}Hf_{0.5}C$ ceramics are amorphous [34]. With increasing heat treatment temperature, only the diffraction peak of β-SiC can be detected due to the crystallization of amorphous $SiTi_{0.2}Zr_{0.3}Hf_{0.5}C$ (Figs. S1(a)–S1(c)). However, no new diffraction peaks assigned to $(Ti_{0.2}Zr_{0.3}Hf_{0.5})C$ can be detected. According to previous work [34], the crystallization of amorphous $SiTi_{0.2}Zr_{0.3}Hf_{0.5}C$ should result in β-SiC and $(Ti_{0.2}Zr_{0.3}Hf_{0.5})C$, respectively. Thus, there should be two sets of diffraction peaks assigned to micro-sized $(Ti_{0.33}Zr_{0.33}Hf_{0.34})C$ and nano-sized $(Ti_{0.2}Zr_{0.3}Hf_{0.5})C$. However, in this work, only one set of diffraction peaks assigned to a new (Ti,Zr,Hf)C phase is detected, and the diffraction peaks of the (Ti,Zr,Hf)C phase gradually shift to lower angles with increasing temperature (Figs. 3(a)–3(c)). This is due to the occurrence of a solid solution reaction between the $(Ti_{0.33}Zr_{0.33}Hf_{0.34})C$ micropowder and the polymer-derived $SiTi_{0.2}Zr_{0.3}Hf_{0.5}C$ ceramics during heat treatment and sintering, resulting in the interdiffusion of Ti, Zr, and Hf. This interesting behavior is not found in the SC-1/2/3 microcomposites.

The diffraction peaks of $(Ti_{0.33}Zr_{0.33}Hf_{0.34})C$ in SC-1/2/3 did not shift during high-temperature annealing, but the diffraction peaks in the sintered SC-1/2/3 samples shifted toward higher angles after sintering (Figs. 3(d)–3(f)). This is because the thermal expansion coefficient of SiC (4.5×10^{-6} K^{-1} [38]) is significantly different from that of TiC (7.7×10^{-6} K^{-1} [39]), ZrC (6.7×10^{-6} K^{-1} [40]), and HfC (6.6×10^{-6} K^{-1} [41]), and thermal mismatch during sintering leads to thermal stress (i.e., lattice strain) in the ceramics. Under the influence of thermal residual stress, both the crystal structures of $(Ti_{0.33}Zr_{0.33}Hf_{0.34})C$ and SiC in the sintered SC samples change slightly. The (Ti,Zr,Hf)C crystals were subjected to compressive stress, so the rightward shift of the (Ti,Zr,Hf)C peak is consistent with this thermal stress theory. To further verify this, the enlarged XRD patterns of SiC are also shown in Fig. S2 in the ESM, which shifted to the left (under tensile stress), which is also consistent with the theory [40,42,43].

All the sintered micro-nano composites and micro composites have a low open porosity of less than 1%. The real molar ratios of Ti, Zr, and Hf in the as-sintered samples were determined via elemental analysis (Table 1). The compositions of the sintered STZHC-1/2/3 are expected to be $(Ti_{0.32}Zr_{0.32}Hf_{0.36})C$/30SiC, $(Ti_{0.32}Zr_{0.32}Hf_{0.36})C$/22SiC, and $(Ti_{0.32}Zr_{0.32}Hf_{0.36})C$/17SiC, respectively. Those for sintered SC-1/2/3 can be expressed as $(Ti_{0.33}Zr_{0.33}Hf_{0.34})C$/30SiC, $(Ti_{0.33}Zr_{0.33}Hf_{0.34})$/22SiC, and $(Ti_{0.33}Zr_{0.33}Hf_{0.34})$/17SiC, respectively. The new metal molar ratios in the as-sintered STZHC-1/2/3 ceramics are attributed to the mutual diffusion of Ti, Zr, and Hf between the $(Ti_{0.33}Zr_{0.33}Hf_{0.34})C$ powders and $SiTi_{0.2}Zr_{0.3}Hf_{0.5}C$ ceramics derived from the $Ti_{0.2}$–$Zr_{0.3}$–$Hf_{0.5}$–VHPCS precursors. Based on Vegard's law [44] and Bragg's equation [19], the diffraction peak of $(Ti_{0.32}Zr_{0.32}Hf_{0.36})C$ in the (111) plane should be approximately 34.05° (in theory), which

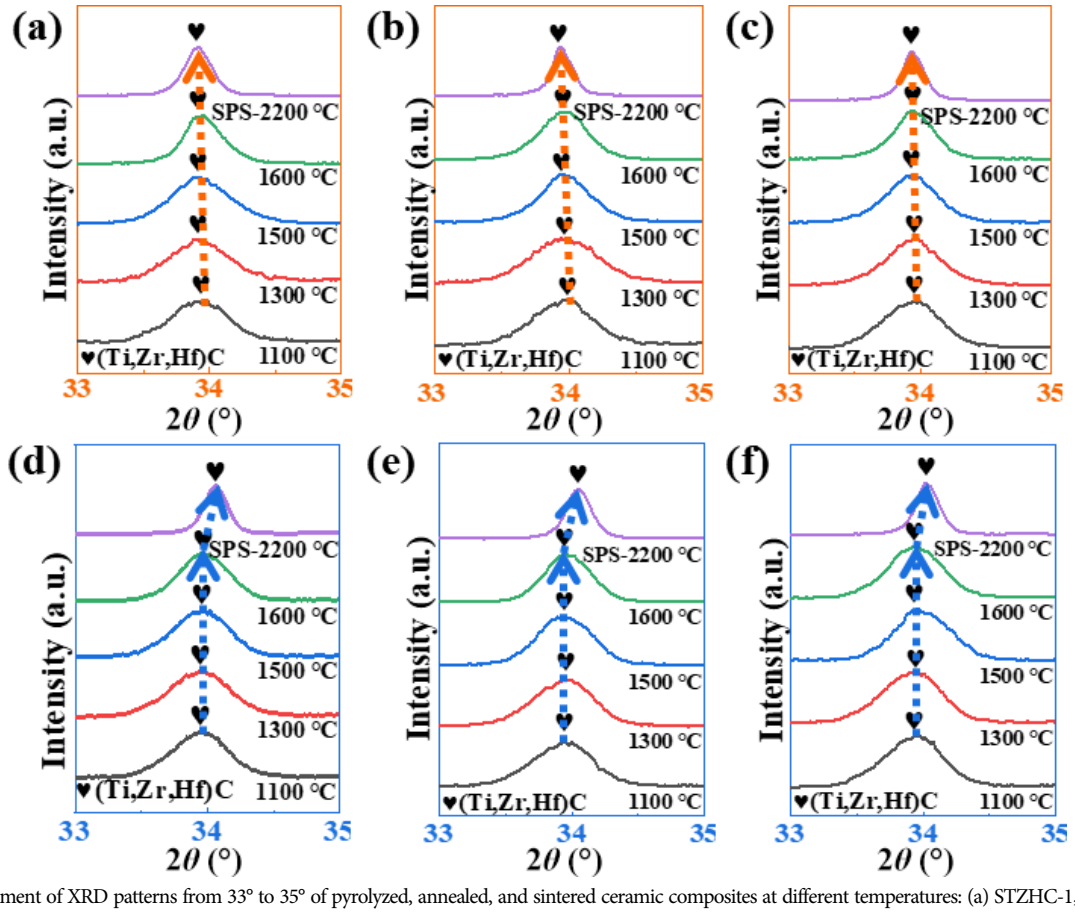

Fig. 3 Enlargement of XRD patterns from 33° to 35° of pyrolyzed, annealed, and sintered ceramic composites at different temperatures: (a) STZHC-1, (b) STZHC-2, (c) STZHC-3, (d) SC-1, (e) SC-2, and (f) SC-3.

is close to the 2θ of 33.94° in the XRD patterns (in fact, Figs. 3(a)–3(c)). This suggests that elemental exchange did occur in the STZHC-1/2/3 samples and that the diffraction peaks of the solid solution carbides indeed shifted to lower angles.

Figure 4 shows SEM images and EDS mappings for Si, Ti, Zr, and Hf elements in the sintered STZHC-1/3 and SC-1/3 samples. The light-colored phases correspond to (Ti,Zr,Hf)C solid solutions, and the dark-colored phases correspond to SiC. In STZHC-1, the (Ti,Zr,Hf)C_{micro} particles are uniformly mixed with (Ti,Zr,Hf)C_{nano}/SiC (Fig. 4(a)). In STZHC-3 samples, the (Ti,Zr,Hf)C_{micro} powders are gradually linked together, forming a micro-nano structure with (Ti,Zr,Hf)C_{nano}/SiC distributed among interconnected (Ti,Zr,Hf)C_{micro} phases (i.e., (Ti,Zr,Hf)C_{micro}/(Ti,Zr,Hf)C_{nano}/SiC structures) (Fig. 4(b)). The microstructures of SC-1/3 are quite different. The added $(Ti_{0.33}Zr_{0.33}Hf_{0.34})C_{micro}$ powders are irregularly distributed in the SiC phases in SC-1 (Fig. 4(c)). As the amount of added powder gradually increases, the structure of SC-3 is formed by a cohesive framework of $(Ti_{0.33}Zr_{0.33}Hf_{0.34})C_{micro}$ carbides with unevenly distributed SiC phases (Fig. 4(d)). Notably, no (Ti,Zr,Hf)C nanograins can be observed in the SiC phases in the (Ti,Zr,Hf)C_{micro}/SiC structure (Figs. 4(c) and 4(d)). The microstructures of STZHC-2 and SC-2 are shown in Fig. S2 in the ESM.

The main reasons for the better uniformity of micro-nano composite ceramics are as follows. The (Ti,Zr,Hf)C phases mixed with SiC phases are divided into three steps. First, $(Ti_{0.33}Zr_{0.33}Hf_{0.34})C$ micropowders are added to VHPCS and homogeneously mixed. A solution containing three metal amides is then titrated into the $(Ti_{0.33}Zr_{0.33}Hf_{0.34})C_{micro}$/VHPCS mixtures at a uniform rate to react with it. The Si–H groups of VHPCS can react with amides by replacing the CH_3 groups, thus promoting the formation of a three-dimensional network structure [34]. The high-viscosity polymers formed during oil bath heating promoted the dispersion of the added $(Ti_{0.33}Zr_{0.33}Hf_{0.34})C_{micro}$ powders and maintained their dispersed state in the STZHC samples. Finally, the mixed solid $Ti_{0.2}$–$Zr_{0.3}$–$Hf_{0.5}$–VHPCS encapsulated with $(Ti_{0.33}Zr_{0.33}Hf_{0.34})C_{micro}$ ceramic powder without sedimentation was obtained in a heated environment with a protective atmosphere. Subsequently, micro-nano composites with multiscale Gobi Desert-like structures were synthesized to synergistically improve the ablation resistance. However, pure VHPCS does not facilitate the formation of high-viscosity polymer-encapsulated $(Ti_{0.33}Zr_{0.33}Hf_{0.34})C_{micro}$ powders before pyrolysis. Therefore, the incorporated $(Ti_{0.33}Zr_{0.33}Hf_{0.34})C_{micro}$ powders cannot be uniformly dispersed in SiC within the SC samples.

According to XRD and microstructural analyses, elemental exchange occurs between the $(Ti_{0.33}Zr_{0.33}Hf_{0.34})C$ microparticles and the $SiTi_{0.2}Zr_{0.3}Hf_{0.5}C$ phase. Thus, the STZHC-1/2/3 samples include micro-nano $(Ti_{0.32}Zr_{0.32}Hf_{0.36})C$. The SC-1/2/3 samples have only microscale $(Ti_{0.33}Zr_{0.33}Hf_{0.34})C$.

To further analyze the microstructure of the micro-nano composites, TEM was carried out on the STZHC-3 sample. HRTEM images, SAED patterns, and EDS mappings were acquired to determine $(Ti_{0.32}Zr_{0.32}Hf_{0.36})C_{micro}$, $(Ti_{0.32}Zr_{0.32}Hf_{0.36})C_{nano}$, and SiC, respectively. In the bright field image (Fig. 5(a)), the $(Ti_{0.32}Zr_{0.32}Hf_{0.36})C_{micro}$ grains with an average size of approximately 1 μm are mixed with $(Ti_{0.32}Zr_{0.32}Hf_{0.36})C_{nano}$/SiC. The average grain size of $(Ti_{0.32}Zr_{0.32}Hf_{0.36})C_{nano}$ in the sample was approximately 70 nm. In the dark field image and EDS mappings (Fig. 5(g)), the Ti, Zr, and Hf elements are distributed uniformly

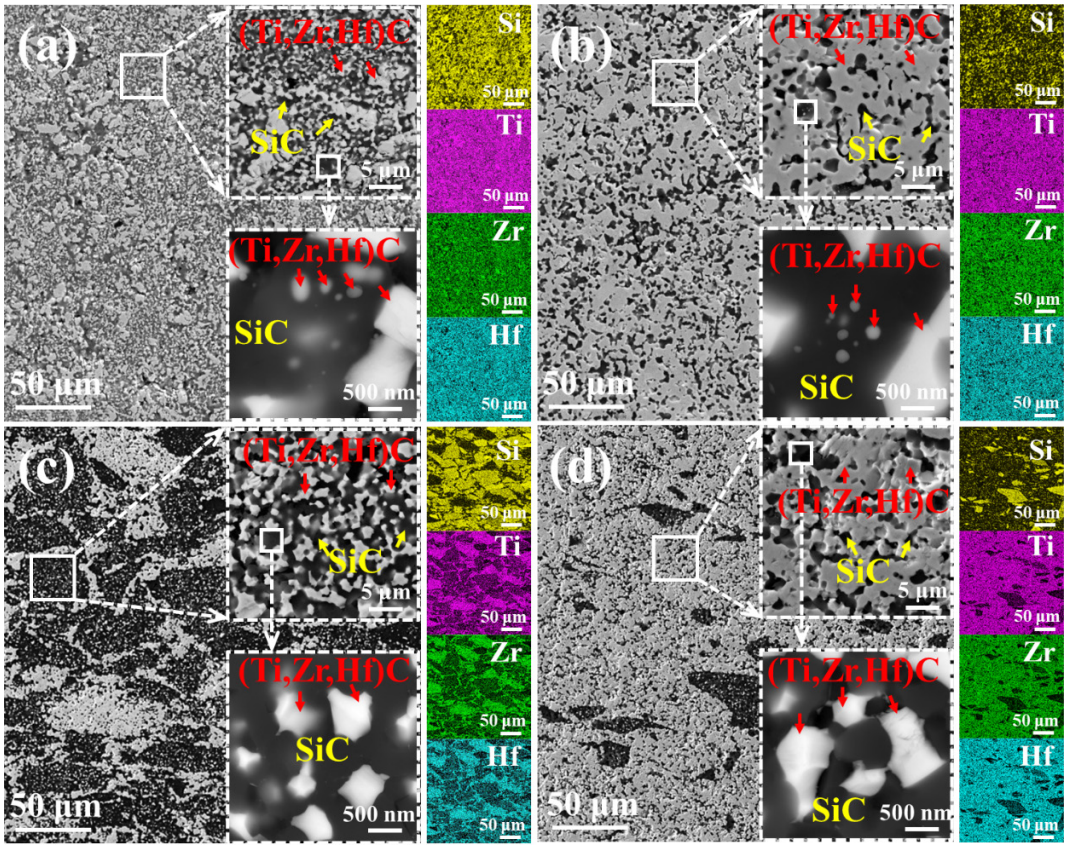

Fig. 4 SEM images and EDS mappings of (a) STZHC-1, (b) STZHC-3, (c) SC-1, and (d) SC-3. Insets show microstructure at high magnifications.

in the light-colored phases ($(Ti_{0.32}Zr_{0.32}Hf_{0.36})C_{micro}$ and $(Ti_{0.32}Zr_{0.32}Hf_{0.36})C_{nano}$), and the Si element is distributed evenly in the dark-colored SiC phases. The C element is distributed throughout the entire mapping. The EDS results of points 1 and 2 (Fig. 5(h)) further confirm that the element exchange phenomenon occurs between (Ti,Zr,Hf)C_{micro} and (Ti,Zr,Hf)C_{nano} powders, resulting in compositions with similar metal ratios.

3.3 Formation process and mechanism of micro-nano structured (Ti,Zr,Hf)C

Based on the experimental results and the discussion above, the formation of micro-nano structured (Ti,Zr,Hf)C can be summarized in two steps as follows (the corresponding formation process is illustrated in Fig. 6(a)):

(1) 1100–1300 °C: According to Ref. [45], the production and migration of vacancies lead to solid solution reactions. The vacancy formation energies of Ti, Zr, and Hf are ranked as Ti (8.6 eV) < Zr (9.3 eV) < Hf (9.4 eV) based on the density functional theory (DFT). Because of the high vacancy formation energies of Ti, Zr, and Hf, solid solution reactions do not occur at low temperatures. The XRD patterns of the $SiTi_{0.2}Zr_{0.3}Hf_{0.5}C$ ceramics (Fig. 6(b)) indicate that the diffraction peaks of the metal carbides steadily shifted toward a lower angle as the temperature increased. This is because Ti, Zr, and Hf have different diffusion rates (Ti > Zr ~ Hf [45]). Ti with a small atomic radius first diffuses from the amorphous phase, followed by Zr and Hf with a large atomic radius to form the solid solution phase [46]. At 1300 °C, although $SiTi_{0.2}Zr_{0.3}Hf_{0.5}C$ remains in an amorphous state, the diffraction peaks of (Ti,Zr,Hf)C in STZHC-1/2/3 slightly shift to lower angles (Figs. 3(a1)–3(c1)), suggesting one-directional diffusion of metallic elements from the amorphous ceramics into $(Ti_{0.33}Zr_{0.33}Hf_{0.34})C$ (Fig. 6(a)). Diffusion is driven by the chemical potential gradient and always results in decreasing free energy [47]. The uniform distribution of metallic elements at the atomic scale can also greatly reduce the activation energy of diffusion [48].

(2) > 1300 °C: SiC diffraction peaks can be observed in the XRD patterns of $SiTi_{0.2}Zr_{0.3}Hf_{0.5}C$ when annealed higher than 1500 °C (Fig. 6(b)), which means that $SiTi_{0.2}Zr_{0.3}Hf_{0.5}C$ undergoes a crystallization process. However, no $(Ti_{0.2}Zr_{0.3}Hf_{0.5})C$ peaks can be detected in the XRD patterns of the $(Ti_{0.32}Zr_{0.32}Hf_{0.36})C$/SiC micro-nano composites, indicating that elemental exchange occurs. More concretely, the crystallization process of $SiTi_{0.2}Zr_{0.3}Hf_{0.5}C$ and the elemental exchange caused by the differences in atomic concentration between $(Ti_{0.2}Zr_{0.3}Hf_{0.5})C_{nano}$ and $(Ti_{0.33}Zr_{0.33}Hf_{0.34})C_{micro}$ occur simultaneously. Interdiffusion of Ti, Zr, and Hf occurs between the micropowders and the polymer-derived nanoceramics and eventually results in a stable state (Fig. 6(a)). Consequently, the obtained $(Ti_{0.32}Zr_{0.32}Hf_{0.36})C_{micro}$ and $(Ti_{0.32}Zr_{0.32}Hf_{0.36})C_{nano}$ in the micro-nano composite ceramics ultimately have the same molar ratio of metal atoms (Table 1).

3.4 Ablation behavior of micro-nano composites and micro composites

Figure 7 displays photographs of the dense sintered composite ceramics after air-plasma ablation at approximately 2200 °C. As illustrated in Fig. 7(a), obvious ablation pits and different ablation regions are evident on the surface of the ablated STZHC-1. There are no obvious ablation pits on the surfaces of STZHC-2 and STZHC-3, but a small amount of oxide peeling can be observed. In contrast, ablation pits and distinct ablation zones can be observed on the surfaces of SC-1 and SC-2, accompanied by yellow oxides and discernible oxide spheres within the ablation center. Additionally, a considerable quantity of oxides detach in

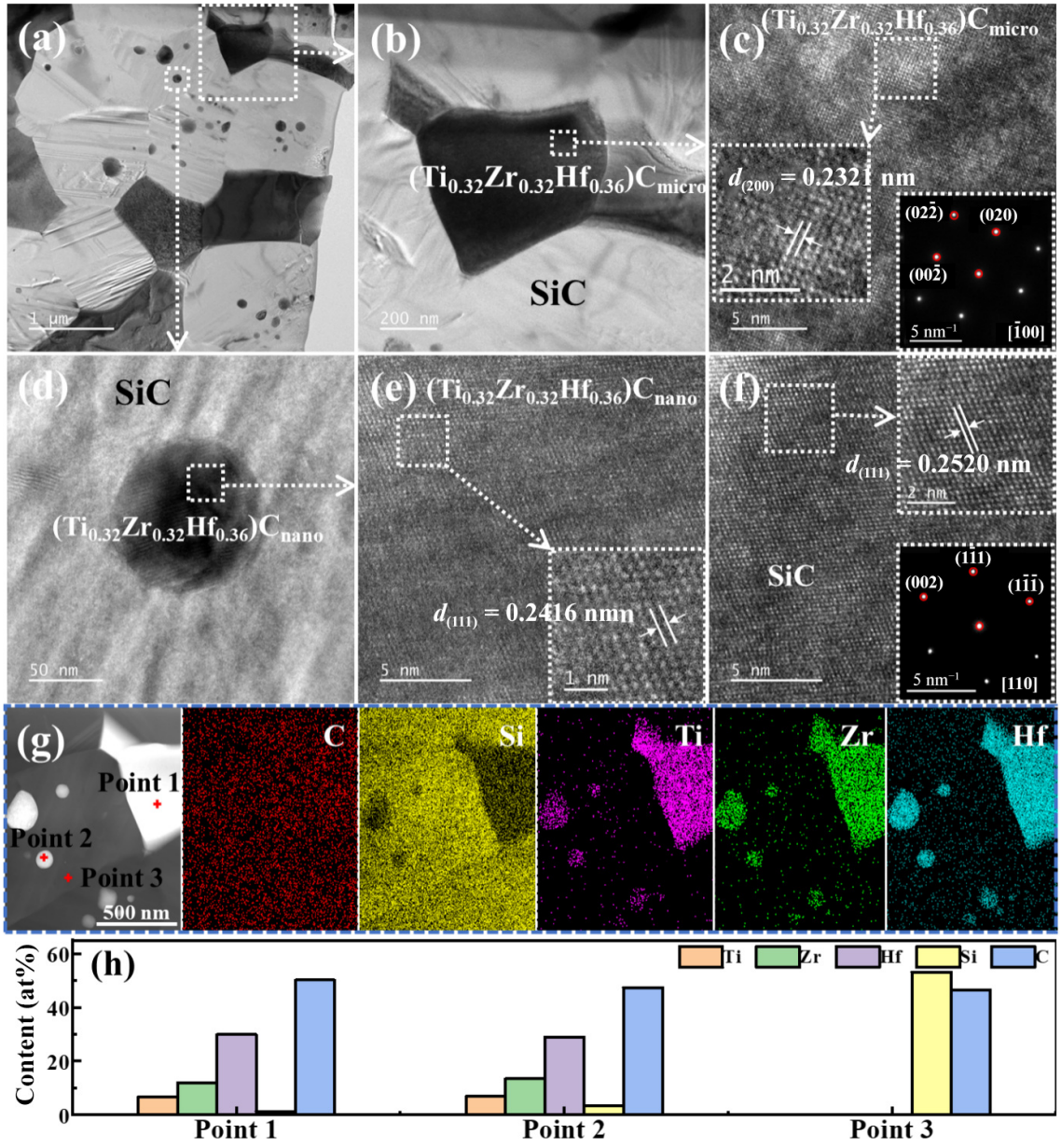

Fig. 5 (a–f) TEM images of sintered STZHC-3 where inserts are the corresponding SAED images; (g) EDS mappings for C, Si, Ti, Zr, and Hf; (h) element contents of points 1–3 in (g).

the transition areas. A notable number of white oxides also fall off the surface of SC-3, exposing the black bulk (Fig. 7(b)). These findings demonstrate that the initial microstructure and phase composition have a significant effect on the surface morphology of the ablated composites. In particular, it is imperative to concurrently employ (Ti,Zr,Hf)C with micro-nano structures and a higher (Ti,Zr,Hf)C content, that is, to prepare an STZHC-3 sample with a multiscale Gobi Desert-like structure to synergistically improve ablation resistance.

Figure 8 displays the ablation curves, ablation rates, and XRD patterns of the ablated ceramic composites. The ablation curves exhibit comparable heating rates, indicating that the surface thermal response behavior of the composite ceramics is analogous (Fig. 8(a)). The maximum surface temperature of micro-nano composites ranges from 2190 to 2250 °C. From the perspective of ablation rates (Fig. 8(b)), the STZHC-3 micro-nano composites and SC-3 micro composite show better ablation performance, with mass and linear ablation rates of −1.01 mg/s and −0.12 μm/s, 0.21 mg/s and 0.32 μm/s, respectively. Notably, the negative ablation rates of STZHC-3 indicate that the mass gain of the oxide layer resulting from oxidation is greater than the mass loss caused by mechanical scouring. Table 2 compares the ablation rates of STZHC-3 and SC-3 with those of other thermal protective ceramics [10,15,42,49,50]. STZHC-3 exhibits excellent ablation performance due to its non-ablative characteristics.

The exceptional ablation resistance of STZHC-3 and SC-3 can be attributed to the high UHTC content (approximately 83 wt%), which is conducive to the formation of a stable oxide skeleton during the high-temperature ablation process. However, with the same UHTC content, the ablation resistance of STZHC-3 is better than that of SC-3, and that of STZHC-2 is better than that of SC-2. This behavior proves that, compared with the microcomposites, the micro-nano composites containing uniformly distributed micro-nano structured (Ti,Zr,Hf)C phases exhibit much better resistance to mechanical scouring caused by high-speed air-plasma. The initial optimized microstructure and protective role of the micro-nano composites are similar to those of the Gobi Desert, where multisized gravels are more effective at

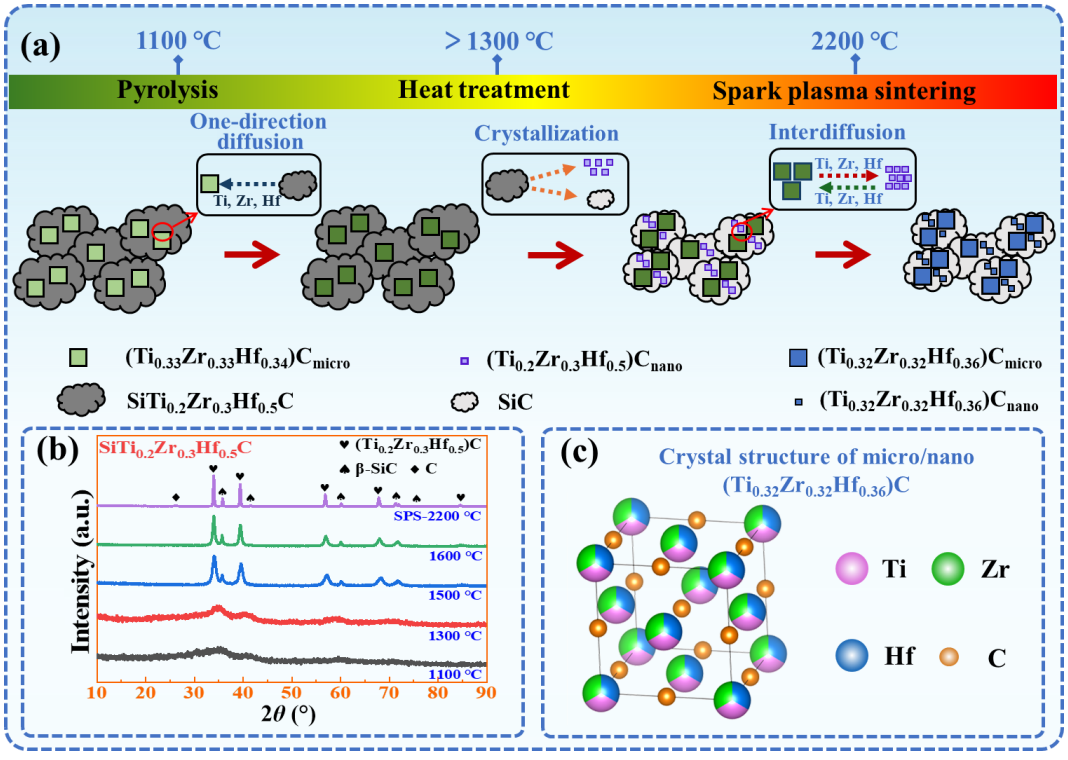

Fig. 6 (a) Schematic diagram of formation process of micro-nano structured (Ti,Zr,Hf)C; (b) XRD patterns of $SiTi_{0.2}Zr_{0.3}Hf_{0.5}C$ ceramics obtained at different temperatures; (c) crystal structure of micro-nano $(Ti_{0.32}Zr_{0.32}Hf_{0.36})C$ ceramics.

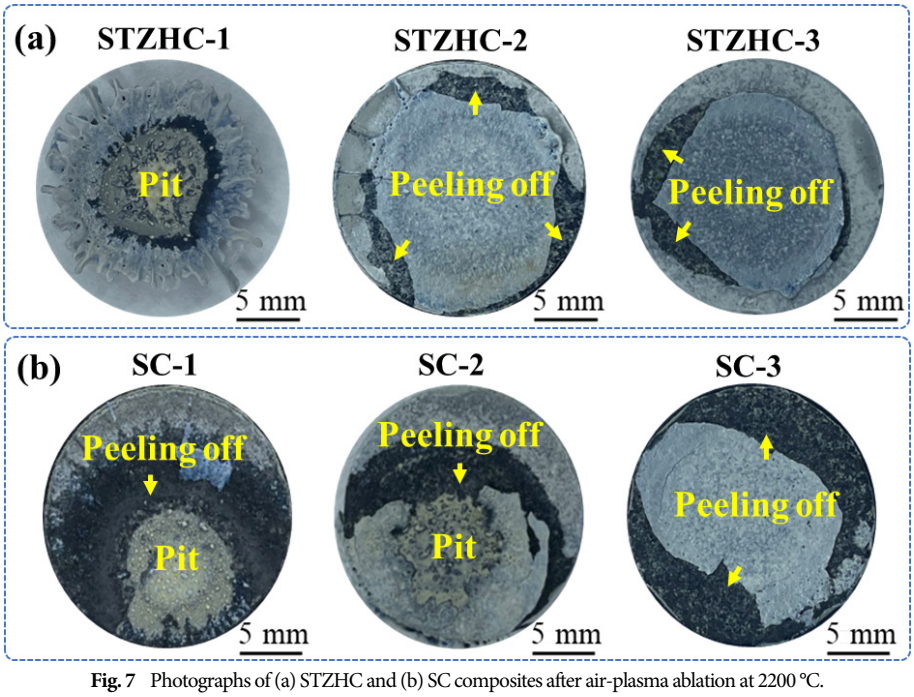

Fig. 7 Photographs of (a) STZHC and (b) SC composites after air-plasma ablation at 2200 °C.

protecting shifting sands from being blown away by strong winds than gravels of only large sizes. The protective role is discussed later.

Figures 8(c) and 8(d) display the XRD patterns of STZHC-1/2/3 and SC-1/2/3 after ablation for 60 s. The phase compositions of the ablated samples are similar to those of the ablated Ti–Zr–Hf–VHPCS-derived ceramic nanocomposites [34]. The XRD peaks are close to those of ZrO_2 (PDF#86-1449), HfO_2 (PDF#74-1506), $ZrTiO_4$ (PDF#34-0415), and $HfTiO_4$ (PDF#40-0794). Moreover, no characteristic peaks are similar to those of TiO_2. Consequently, a new oxide solid solution phase $(Ti,Zr,Hf)O_2$ appeared after ablation. In addition, TiO_2 reacted with ZrO_2 and HfO_2, resulting in the formation of $(Zr,Hf)TiO_4$.

The surface morphologies of the ablated central regions of the STZHC-1/2/3 micro-nano composites were characterized via SEM (Fig. 9). The ablation surface of STZHC-1 exhibits irregularly distributed $(Ti,Zr,Hf)O_2$ (Fig. 9(a)), whereas that of STZHC-2 displays an increased oxide content with a diffuse and incoherent distribution (Fig. 9(b)). As the (Ti,Zr,Hf)C content increased, the amount of $(Ti,Zr,Hf)O_2$ oxides in STZHC-3

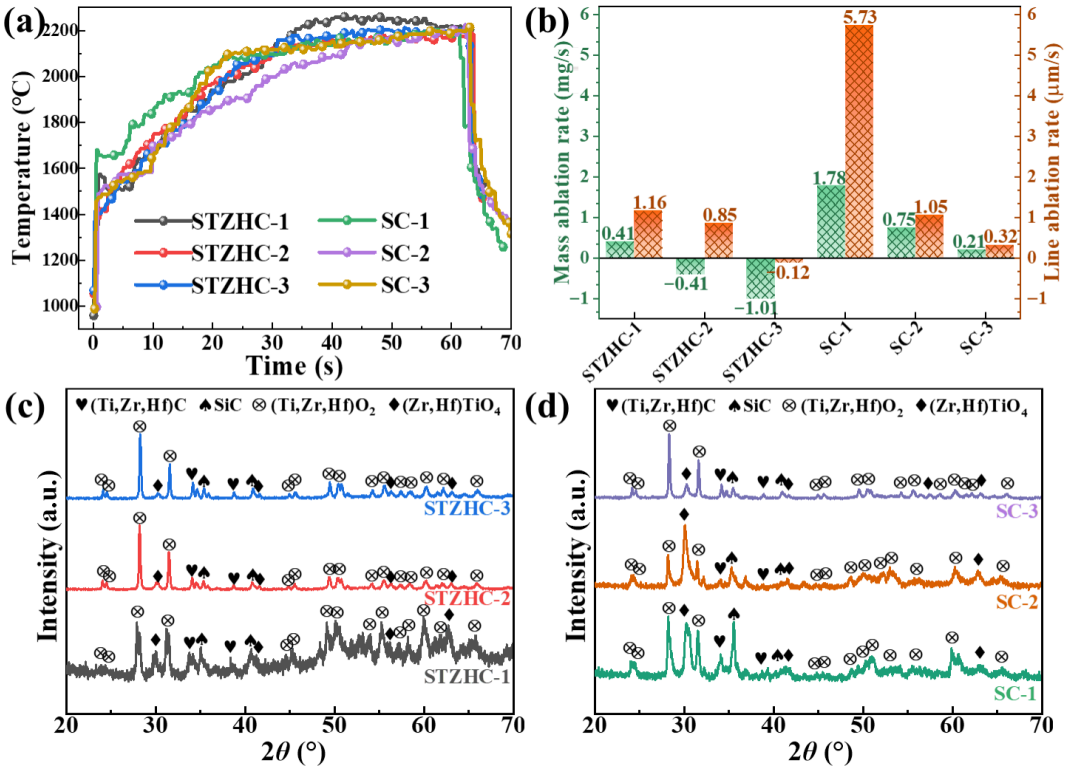

Fig. 8 (a) Ablation curves, (b) ablation rates, and (c, d) XRD patterns of the ablated STZHC and SC composites.

Table 2 Mass ablation rate (R_m) and linear ablation rate (R_l) of samples in this work and other studies under similar ablation conditions

Sample	Ablation test	R_m (mg/s)	R_l (μm/s)	Ref.
$Ta_{0.5}Hf_{0.5}C$	Plasma flame, 2200 °C, 30 s	0.67	2.38	[50]
(Hf–Ta–Zr–Nb)C	Plasma flame, 2186 °C, 60 s	0.66	8.5	[10]
$(Hf_{0.2}Zr_{0.2}Ta_{0.2}Nb_{0.2}Ti_{0.2})C$	Oxy-acetylene flame, 2227 °C, 60 s	33.8	23.6	[49]
(Hf–Ta–Zr–Nb–Ti)C	Plasma flame, 2157 °C, 90 s	–	3.1	[15]
(Hf–Ta–Zr–Nb–Ti)C–20 vol%SiC	Plasma flame, 2063 °C, 90 s	–	1.6	[15]
(TiZrHfNbTa)C–SiC	Oxy-acetylene flame, 2000 °C, 120 s	1.9	2.1	[42]
SC-3	Plasma flame, 2200 °C, 60 s	0.21	0.32	This work
STZHC-3	Plasma flame, 2202 °C, 60 s	−1.01	−0.12	This work

dramatically increased, and the microscale (Ti,Zr,Hf)O_2 was interconnected and formed a network-like skeleton (Fig. 9(c)). Interestingly, the (Ti,Zr,Hf)O_2 skeleton is an integrated high-strength structure that can provide a framework in the oxide layer [51,52]. Studies have shown that the structure remains intact even when cracks are created or progressively expand in the network structure [52]. The formation of this unique protective oxide layer is due to the micro-nano structure of STZHC-3, with (Ti,Zr,Hf)C_{nano}/SiC distributed among the (Ti,Zr,Hf)C_{micro} phase. The network-like (Ti,Zr,Hf)O_2 skeleton is derived from the interconnected $(Ti_{0.32}Zr_{0.32}Hf_{0.36})C_{micro}$ particles, which can increase the resistance of the oxide layer to mechanical scouring and improve the high-temperature stability of the oxide layer. Insufficient carbide content prevents the formation of stable and uniformly distributed (Ti,Zr,Hf)O_2 oxides on the STZHC-1/2 surface. Additionally, many pores and pinholes caused by escaping CO and SiO gases can be observed on the surface [53] (Figs. 9(a) and 9(b)).

The EDS images clearly reveal significant elemental segregation in the oxides on the surfaces of STZHC-2 and STZHC-3 (Figs. 9(d) and 9(e)). The oxide particles are surrounded predominantly by Ti, while the interior is Hf/Zr-rich. This behavior is related to the thermodynamic properties of the metal in the UHTCs [54]. The preferentially oxidized components will migrate and form a Zr, Hf-rich oxidized skeleton [55]. Moreover, the laggingly oxidized elements evolve into Ti-rich oxides that fill the skeleton [56]. Hence, it can be further inferred, combined with the XRD results, that the white oxides are (Ti,Zr,Hf)O_2, and the filling phases include (Zr,Hf)TiO_4 and SiO_2.

Moreover, many (Ti,Zr,Hf)O_2 nanograins appear in the liquid SiO_2/(Zr,Hf)TiO_4 phases (Figs. 9(b2) and 9(c2)). In previous work [34], polymer-derived ceramics were shown to form a protective oxide layer comprising glassy SiO_2 and nano-(Ti,Zr,Hf)O_2. The (Ti,Zr,Hf)O_2 nanoparticles exhibit a pinning effect in adjusting the viscosity of the glassy phases, further hindering the diffusion of oxygen atoms and enhancing their ablation performance. TEM analysis was performed to further clarify the microstructure and composition of the nanosized oxides in STZHC-3 (Fig. 10). The sizes of the large (Ti,Zr,Hf)O_2 grains range from 80 to 100 nm, and the small (Ti,Zr,Hf)O_2 grains range from 10 to 20 nm. According to the EDS results (Fig. 10(d)), the white particles are enriched with Ti, Zr, and Hf. Si and O are uniformly distributed throughout the entire region. The interplanar spacing measured from the HRTEM images in Fig. 10(b) is 0.2512 nm, which is in

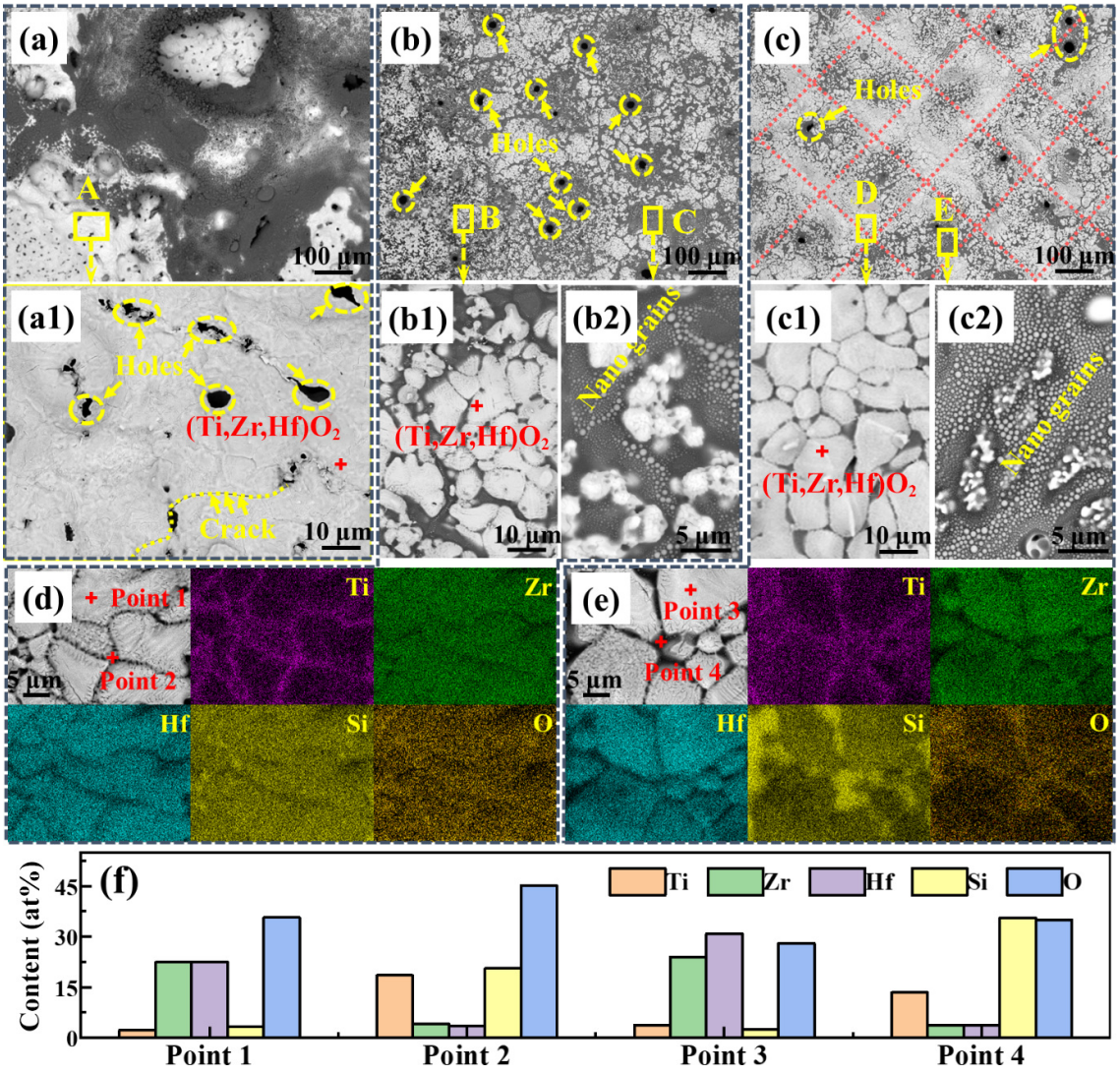

Fig. 9 SEM images of central region of ablated STZHC samples: (a, a1) STZHC-1, (b, b1, b2) STZHC-2, (c, c1, c2) STZHC-3; EDS mappings for Ti, Zr, Hf, Si, and O in (d) STZHC-2 and (e) STZHC-3; (f) element contents of points 1–4 in (d, e).

accordance with the spacing of the (002) planes of $(Ti,Zr,Hf)O_2$ with the space group P21/c. The interplanar spacing in Fig. 10(c) is 0.2875 nm, which corresponds to the $(\bar{1}11)$ planes of $(Ti,Zr,Hf)O_2$. Thus, the EDS and HRTEM results further confirmed that both the larger and smaller nano-oxides are $(Ti,Zr,Hf)O_2$. The larger nanoparticles may be derived from the *in situ* oxidation of $(Ti_{0.32}Zr_{0.32}Hf_{0.36})C_{nano}$, whereas the smaller nanograins are precipitated because of molten evaporation during the ablation process and subsequent cooling to room temperature [57]. The smaller grains diffuse toward the larger nano-$(Ti,Zr,Hf)O_2$ particles and participate in their growth [58]. According to percolation threshold theory [59], when the size of the dispersed $(Ti,Zr,Hf)O_2$ is on the nanoscale, particularly less than 50 nm, only a small number of nanophases (< 5 vol%) will be enough to form a continuous network within the molten matrix, facilitating the formation of a dense and stable oxide layer.

Therefore, the excellent ablation resistance of STZHC-3 is attributed to the special structure of the oxide layer, which comprises microscale $(Ti,Zr,Hf)O_2$ skeletons derived from $(Ti_{0.32}Zr_{0.32}Hf_{0.36})C_{micro}$ and liquid $SiO_2/(Zr,Hf)TiO_4$ matrix phases with uniformly dispersed $(Ti,Zr,Hf)O_2$ nanoparticles derived from $(Ti_{0.32}Zr_{0.32}Hf_{0.36})C_{nano}$. The microscale $(Ti,Zr,Hf)O_2$ skeletons and $(Ti,Zr,Hf)O_2$ nanoparticles protected the liquid $(Zr,Hf)TiO_4$ and SiO_2 phases from being blown away by air-plasma, similar to gravels of various sizes stabilizing shifting sands in the Gobi Desert.

The surface morphologies of transitional and edge regions of the ablated STZHC-1/2/3 composites are shown in Fig. S3 in the ESM and Fig. 11. The aggregated $(Ti,Zr,Hf)O_2$ particles and $SiO_2/(Zr,Hf)TiO_4$ demonstrated the occurrence of liquid sintering (Fig. 11(a)). The surface of STZHC-3 is flat, and the distribution of oxides is related to the path of the airflow, indicating that the oxides can remain stable under high-velocity airflow (Fig. S3(c) in the ESM). The enlarged image of the white oxides shows that the oxide particles are tightly bonded to each other (Figs. 11(b) and 11(c)). Many nanoscale chain-like $(Ti,Zr,Hf)O_2$ can also be observed (Figs. 11(b1) and 11(c1)). The coexistence of micro- and nano-oxides facilitates the formation of a more stable oxide layer, which is consistent with their low linear ablation rates and negative mass ablation rates. In general, the ablation edge region has lower temperatures and weaker mechanical scouring. Consequently, the oxide contents of the edge regions were analyzed in combination with their microstructures, as shown in Fig. 7, and their ablation rates. The positive ablation rates of STZHC-1 indicate that the relatively dense oxide layer of the edge region is related to the strong scouring of the oxides by the air

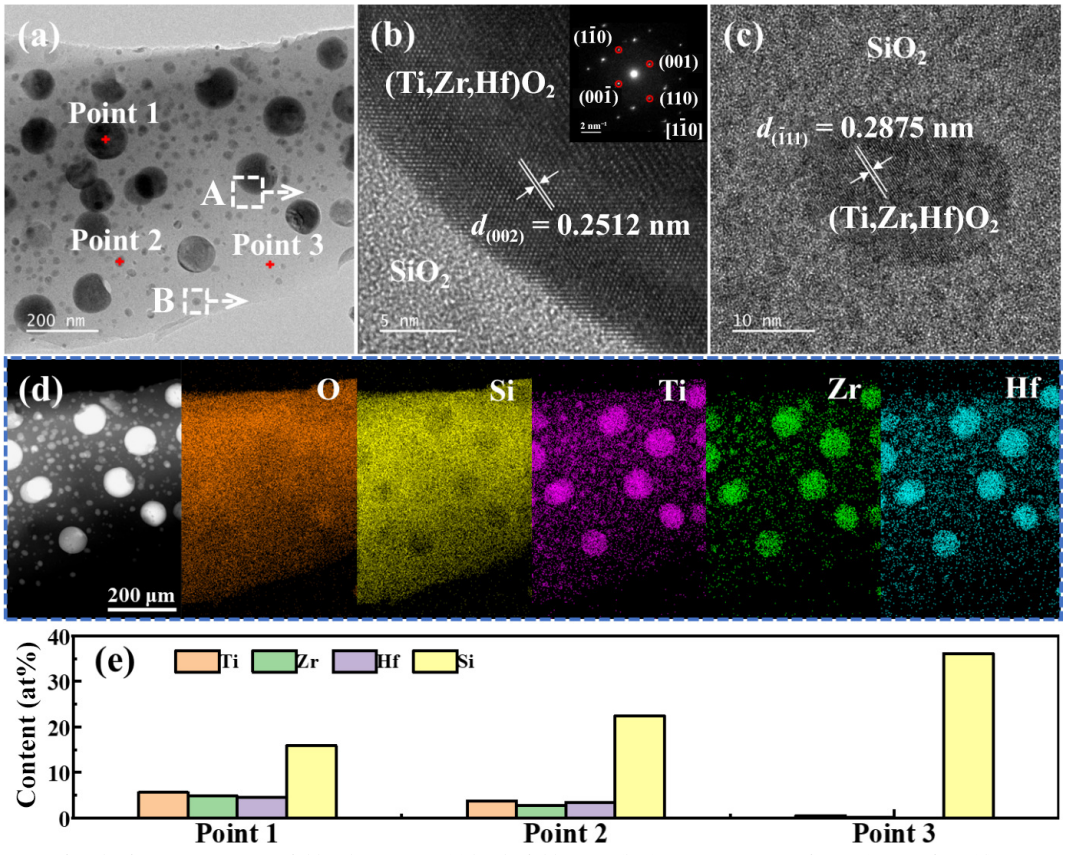

Fig. 10 TEM images of oxides from center region of ablated STZHC-3: (a) bright field image; (b, c) HRTEM images of nano-(Ti,Zr,Hf)O_2; (d) EDS mappings for O, Si, Ti, Zr, and Hf. (e) Element contents of points 1–3 in (a).

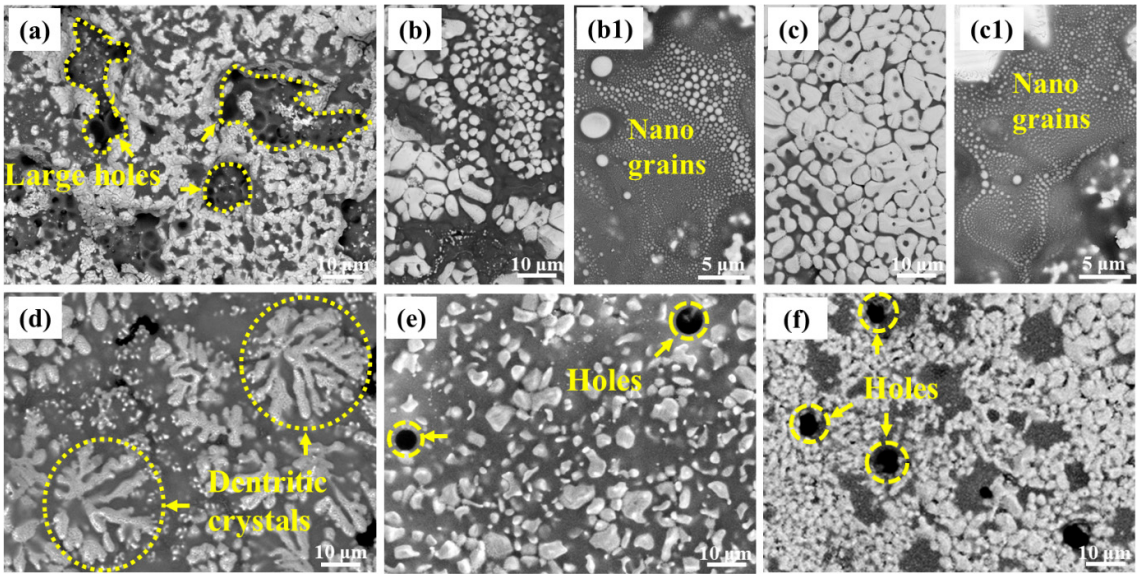

Fig. 11 Enlarged surface SEM images of ablated samples: transitional regions (a) STZHC-1, (b, b1) STZHC-2, (c, c1) STZHC-3; edge regions (d) STZHC-1, (e) STZHC-2, (f) STZHC-3.

flow in the center region. The porous surfaces of STZHC-2/3 indicate that fewer oxides were blown to the edge regions and further demonstrate that the micro- and nanosized high-melting-point (Ti,Zr,Hf)O_2 oxides play a vital role in stabilizing the liquid SiO_2/(Zr,Hf)TiO_4 phases. Furthermore, Zhang *et al.* [35] have reported that interdiffusion behavior can occur between (Ti,Zr,Hf)O_2 and SiO_2 to form (Ti,Zr,Hf)$_x$Si$_y$O$_z$ glass in the ablation transition region, reducing the evaporation of SiO_2 and preventing the penetration of oxygen.

The surface morphologies of the ablated SC-1/2/3 composites were also investigated (Fig. 12 and Fig. S4 in the ESM). Compared with the micro-nano composites in Fig. 9, agglomerated SiO_2 and loose (Ti,Zr,Hf)O_2 can be observed on the surface of SC-1/2, and unfilled pores are present on the surface of SC-3 (Figs. 12(a)–12(c)). Owing to the absence of metal amides in the precursors, the simple pure VHPCS does do not facilitate the formation of high-viscosity polymer-encapsulated $(Ti_{0.33}Zr_{0.33}Hf_{0.34})C_{micro}$ powders; therefore, the $(Ti_{0.33}Zr_{0.33}Hf_{0.34})C_{micro}$ powders cannot be

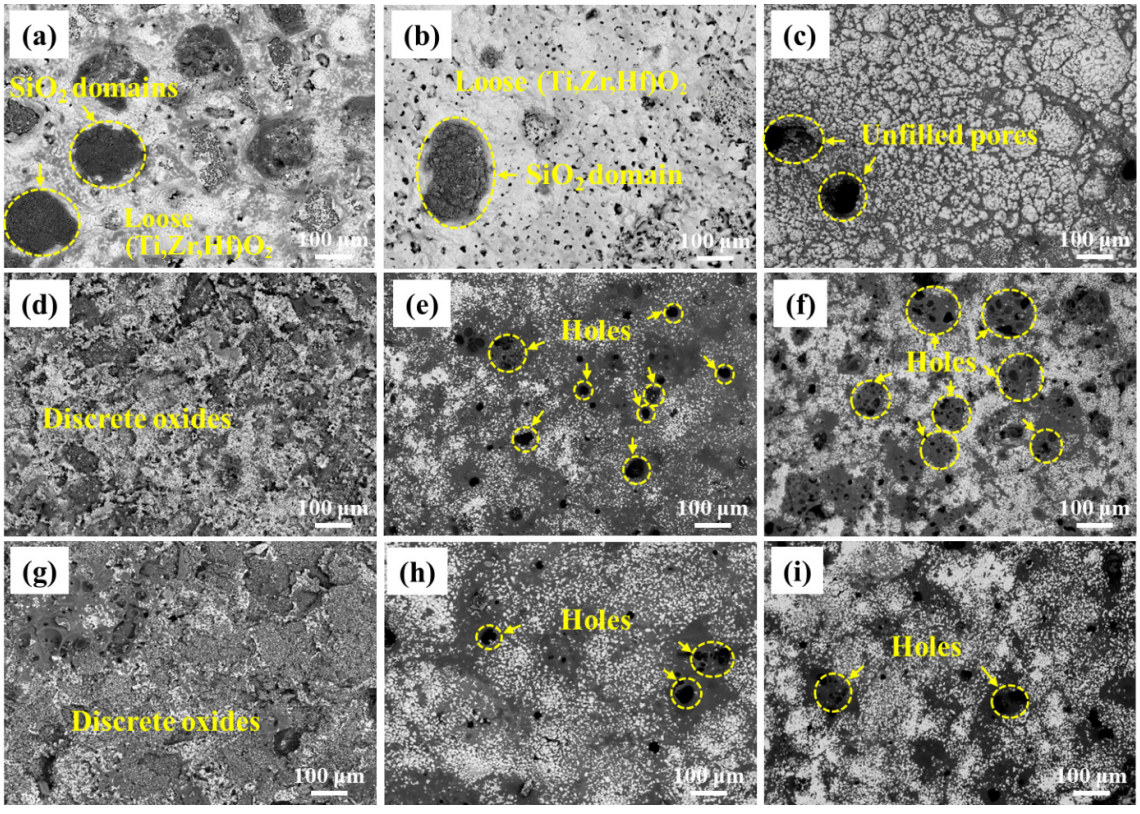

Fig. 12 Surface SEM images of ablated central region: (a) SC-1, (b) SC-2, and (c) SC-3; transitional region: (d) SC-1, (e) SC-2, and (f) SC-3; and edge region: (g) SC-1, (h) SC-2, and (i) SC-3.

uniformly dispersed in the SiC (which is derived from VHPCS) in the SC samples. Consequently, the oxidation of concentrated SiC results in the formation of SiO_2 domains, which do not contain metallic oxides. The SiO_2 domains can be easily blown away and leave only loose $(Ti,Zr,Hf)O_2$ in the central region (Figs. 12(a) and 12(b)). The transition and edge regions of SC-1 also exhibit a considerable number of discrete white oxide particles (Figs. 12(d) and 12(g)). However, they cannot form a protective layer, thereby leading to exposure of the underlying matrix. SC-3 shows the best ablation performance among the three microcomposites, but its oxide layer is significantly less stable than that of STZHC-3. Compared with those in STZHC-3, the $(Ti,Zr,Hf)O_2$ oxides at the center of SC-3 aggregate into isolated island-like structures rather than network-like structures because of the absence of pinned $(Ti,Zr,Hf)O_2$ nanoparticles derived from $(Ti,Zr,Hf)C_{nano}$ (Fig. S4(c) in the ESM).

Both STZHC-3 and SC-3 contain approximately 83 wt% (Ti,Zr,Hf)C, but their different micro-nano or micro-(Ti,Zr,Hf)C structures lead to different ablation rates and microstructures. The micro-nano $(Ti_{0.32}Zr_{0.32}Hf_{0.36})C$ phases are relatively uniformly distributed, with SiC matrix phases in the as-sintered STZHC-3. The substantial quantity of $(Ti_{0.32}Zr_{0.32}Hf_{0.36})C_{micro}$ powder serves as the primary skeleton, with the polymer-derived $(Ti_{0.32}Zr_{0.32}Hf_{0.36})C_{nano}$/SiC phases uniformly spread out in the interstitial space of the skeleton, similar to the multiscale gravels with fine sands in the Gobi Desert model. The $(Ti_{0.32}Zr_{0.32}Hf_{0.36})C_{micro}$ powders subsequently formed a microscale $(Ti,Zr,Hf)O_2$ network-like skeleton during the ablation process in the STZHC-3, and the nano-$(Ti,Zr,Hf)O_2$ oxides derived from $(Ti_{0.32}Zr_{0.32}Hf_{0.36})C_{nano}$ throughout the liquid SiO_2/$(Zr,Hf)TiO_4$ phase matrix significantly improved the stability of the oxide layer.

However, there are clear (Ti,Zr,Hf)C-aggregated and SiC-enriched zones in the as-sintered SC-3. Owing to the lack of polymer-derived (Ti,Zr,Hf)C nanoparticles, it is unable to generate *in situ* nano-$(Ti,Zr,Hf)O_2$ oxides during the ablation process. Although *ex situ* nanosized $(Ti,Zr,Hf)O_2$ oxides can also be observed on the surface of SC-3 (Figs. S4(j)–S4(l) in the ESM), their formation mechanism determines their role in the ablation process. The nanosized $(Ti,Zr,Hf)O_2$ oxides on the surface of SC-3 are supersaturated precipitates caused by melt evaporation during the subsequent cooling process [57] and cannot enter the molten oxides to stabilize them. Owing to the lack of pinning effect of the $(Ti,Zr,Hf)O_2$ nanoparticles on the molten phases in SC-3, the oxidized micro $(Ti,Zr,Hf)O_2$ will be subjected to high tensile stress caused by mechanical erosion during the ablation process and will not be able to form a continuous network-like skeleton, which ultimately exists in the isolated island-like structures. The presence of *in situ* $(Ti,Zr,Hf)O_2$ nanoparticles (derived from $(Ti,Zr,Hf)C_{nano}$) can optimize the structure of the oxide layer, which also demonstrates the superiority of the optimized Gobi Desert structure (i.e., multisized gravels). The synergistic effect of a high-content UHTC with micro-nano structures plays a crucial role in improving the stability of the oxide layer and enhancing the ablation resistance of the materials.

The cross-sectional morphologies of the ablated samples are shown in Fig. 13. The oxide layer of the STZHC-1/2/3 micro-nano composite ceramics is more complete than that of the SC-1/2/3 microcomposites, and more white $(Ti,Zr,Hf)O_2$ oxides are present on the ablated micro-nano composites. A large penetrating crack appears between the oxide layer and the substrate of STHZC-1, causing severe separation of the two parts. The small thickness of the oxide layer is due to the spalling that takes place by mechanical scouring during ablation (Fig. 13(a)). This indicates that the deficiency of the $(Ti,Zr,Hf)O_2$ skeleton (derived from $(Ti_{0.32}Zr_{0.32}Hf_{0.36})C_{micro}$) hinders the stability of the oxide layer. As the (Ti,Zr,Hf)C content in STZHC-3 increases, a

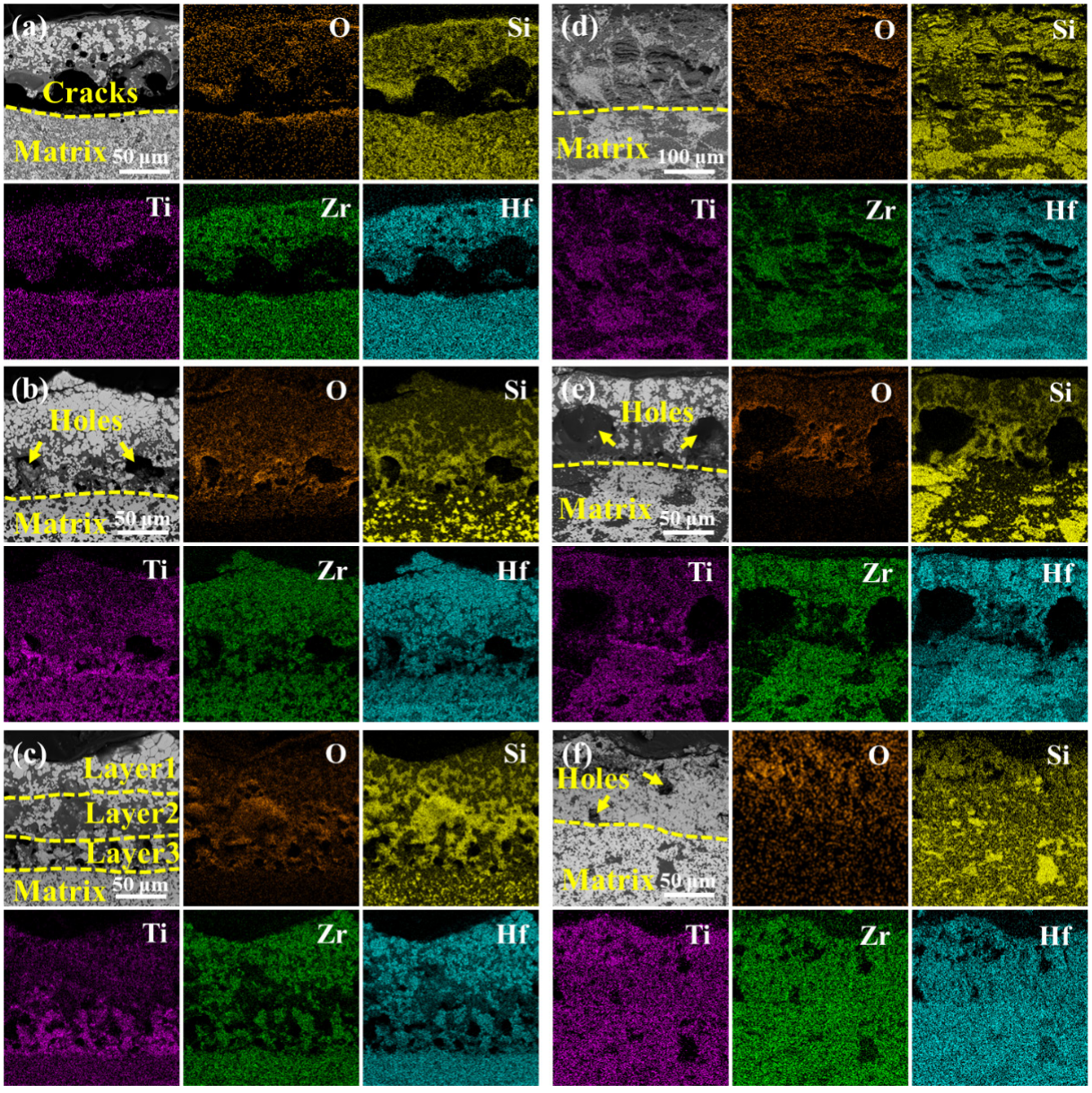

Fig. 13 Cross-sectional SEM images of ablated samples: (a) STZHC-1, (b) STZHC-2, (c) STZHC-3, (d) SC-1, (e) SC-2, and (f) SC-3.

high-strength network-like skeleton is formed with sufficient $(Ti,Zr,Hf)O_2$ nanoparticles that protect the liquid SiO_2/$(Zr,Hf)TiO_4$ phases (Fig. 13(c)). This further stabilized the oxide layer from being stripped by the high-velocity airflow. This is consistent with the nonablative characteristics exhibited by STZHC-3 in Fig. 8(b), with mass and linear ablation rates of −1.01 mg/s and −0.12 μm/s, respectively, indicating that its mass and thickness increase after the high-temperature ablation process. However, in SC-3, a relatively high content of micro $(Ti,Zr,Hf)O_2$ is aggregated in the form of an isolated island (Fig. 12(c)), which could not effectively protect the liquid phase matrix during the high-temperature air-plasma test (Fig. 13(f)). This also corresponds to its positive mass and linear ablation rates (0.21 mg/s and 0.32 μm/s, Fig. 8(b)).

Accurately, the oxide layer in the STZHC-3 has a three-layered structure as follows (Fig. 13(c)): layer 1: dense outer layer; layer 2: dense Si-rich layer; and layer 3: Ti, Zr, Hf-rich inner layer. The micro-$(Ti,Zr,Hf)O_2$ skeleton, nano-$(Ti,Zr,Hf)O_2$, and liquid SiO_2/$(Zr,Hf)TiO_4$ make up the dense outer layer (layer 1), which is associated with its Gobi Desert structure and can effectively avoid the loss of liquid phases. The dense Si-rich layer may be related to the active oxidation of the SiC matrix, with the generated SiO further oxidizing when it escapes outward. This also highlights the protective effect of the dense and stable outer layer 1 with low oxygen permeability, which keeps the oxygen partial pressure in the internal layer low [60]. Layer 2 also functions as a connecting link between layers 1 and 3. It not only repairs the defects of outer layer 1 but also impedes the inward penetration of oxygen atoms. Layer 3 connects the Si-rich layer and the matrix to ensure the stability of the oxide layer, which can be evidenced by its negative ablation rates. In addition, layer 3 serves as a buffer layer to relieve the thermal stresses caused by the thermal expansion mismatch between the oxide and the matrix.

3.5 Mechanism of ablation resistance enhancement of micro-nano composites

A schematic diagram of the ablation mechanisms of the (Ti,Zr,Hf)C/SiC micro-nano composites and micro composites is

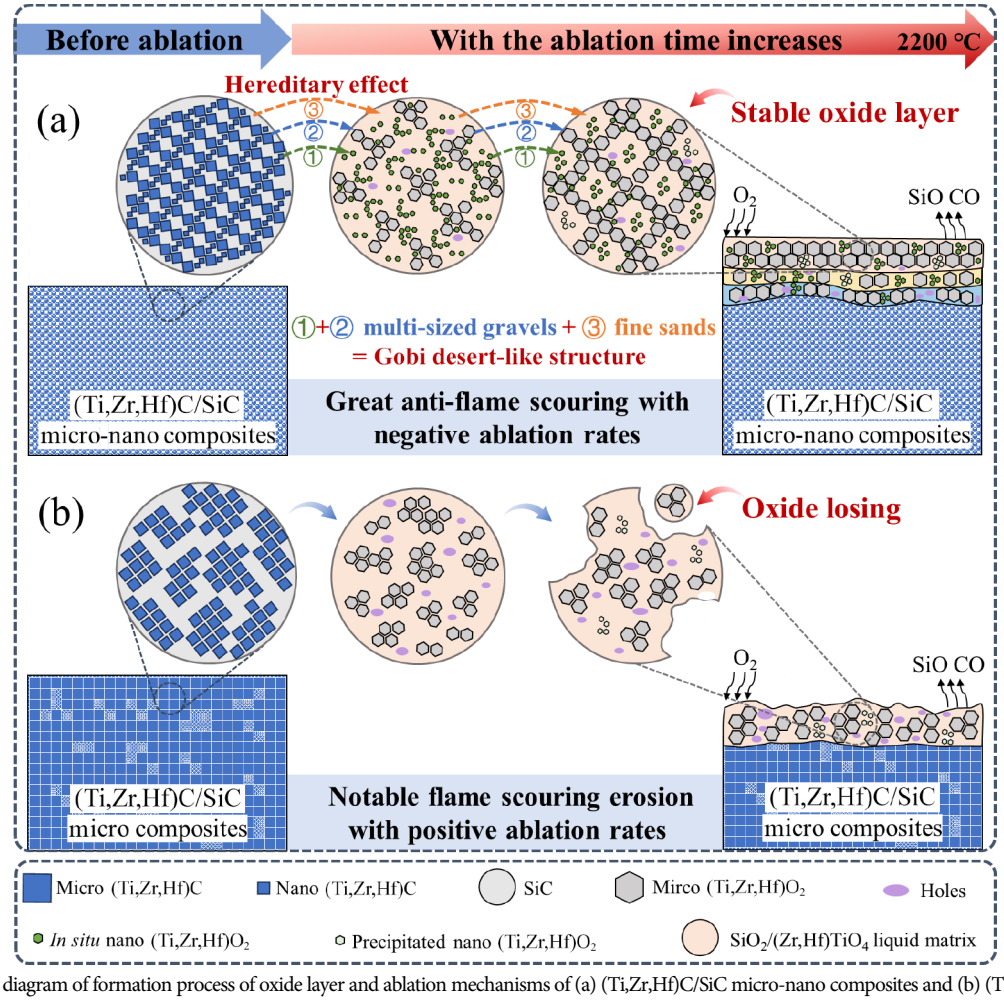

Fig. 14 Schematic diagram of formation process of oxide layer and ablation mechanisms of (a) (Ti,Zr,Hf)C/SiC micro-nano composites and (b) (Ti,Zr,Hf)C/SiC micro composites.

shown in Fig. 14. In the micro-nano composites (i.e., STZHC-3), as the added $(Ti_{0.33}Zr_{0.33}Hf_{0.34})C_{micro}$ powders increase, they gradually link together, forming a multiscale Gobi Desert-like structure with $(Ti_{0.32}Zr_{0.32}Hf_{0.34})C_{nano}$/SiC distributed among interconnected $(Ti_{0.32}Zr_{0.32}Hf_{0.34})C_{micro}$ phases. During the initial ablation stage, the $(Ti,Zr,Hf)C_{micro}$ particles undergo oxidation, and their oxides slightly grow, forming microscale $(Ti,Zr,Hf)O_2$ oxide clusters. Moreover, the nano-$(Ti,Zr,Hf)O_2$ oxides aggregate and form chain-like structures between the micro-$(Ti,Zr,Hf)O_2$ grains. As the ablation time increases, the micro-$(Ti,Zr,Hf)O_2$ oxides continue to grow, while the aggregated nano-$(Ti,Zr,Hf)O_2$ oxides also grow and connect with microsized oxides to form a stable and network-like oxide framework (Fig. 14(a)). The Gobi Desert-like micro-nano structure can be preserved in the oxide layer due to the hereditary effects of the material structure in the (Ti,Zr,Hf)C/SiC micro-nano composites. A stable and dense oxide layer featuring a unique structure consisting of a highly stable $(Ti,Zr,Hf)O_2$ oxide skeleton derived from $(Ti_{0.32}Zr_{0.32}Hf_{0.36})C_{micro}$ and uniformly dispersed nano-(Ti, Zr, Hf)O_2 particles in the liquid SiO_2/$(Zr,Hf)TiO_4$ phases derived from $(Ti_{0.32}Zr_{0.32}Hf_{0.36})C_{nano}$/SiC formed. $(Ti,Zr,Hf)O_2$ can enhance the resistance of the oxide layer to mechanical scouring during ablation. In addition, the homogeneously dispersed nano-$(Ti,Zr,Hf)O_2$ particles improved the viscosity of the liquid phase matrix by pinning effects. The liquid phases hinder the transportation of oxygen, further improving the oxidation and ablation resistance of the micro-nano composites. The microscale $(Ti,Zr,Hf)O_2$ skeleton and $(Ti,Zr,Hf)O_2$ nanoparticles protected the liquid $(Zr,Hf)TiO_4$ and SiO_2 phases from being blown away by air-plasma, similar to gravels of various sizes, which stabilized shifting sands in the Gobi Desert. The shifting sands filled the gaps between the gravels, preventing further wind erosion of the multisized gravels and the underlying substrate. This protective oxide layer shows great anti-flame scouring, and thus, the micro-nano composites show great ablation resistance with negative ablation rates (increased weight and thickness).

However, in the microcomposites (i.e., SC-3), as the amount of added powder gradually increased, aggregated $(Ti,Zr,Hf)C_{micro}$ carbides with nonuniformly distributed SiC phases formed. The uneven $(Ti,Zr,Hf)C_{micro}$ particles oxidize to form isolated island-like micro-$(Ti,Zr,Hf)O_2$ oxides, which grow larger as the ablation time increases. Owing to the lack of connected *in situ* nano-$(Ti,Zr,Hf)O_2$ oxides, no stable network-like micro-$(Ti,Zr,Hf)O_2$ oxide skeletons are formed during the high-temperature ablation process (Fig. 14(b)). The oxide layer exhibited weak resistance to mechanical scouring from the flame. Therefore, notable flame scouring erosion and oxide loss can be observed, and the microcomposite exhibits positive ablation rates (decreased weight and thickness).

4 Conclusions

Inspired by the Gobi Desert's wind-resistant gravel-stabilized sand structure, (Ti,Zr,Hf)C/SiC micro-nano composites with varying (Ti,Zr,Hf)C contents (70, 78, and 83 wt%) were synthesized by

combining the PDC and SSR methods. The micro-nano composites showed distinct grain sizes of approximately 1 μm for (Ti,Zr,Hf)C_{micro} and approximately 70 nm for (Ti,Zr,Hf)C_{nano}, while exhibiting nearly identical metal atomic ratios (Ti : Zr : Hf = 0.32 : 0.32 : 0.34) resulting from elemental interdiffusion during heat treatment. The STZHC-3 and SC-3 composites with similar high (Ti,Zr,Hf)C contents exhibited enhanced ablation performance at approximately 2200 °C, with mass and linear ablation rates of −1.01 mg/s and −0.12 μm/s, 0.21 mg/s and 0.32 μm/s, respectively. The negative ablation rates of STZHC-3 suggest the formation of highly stabilized and protective oxide layers on its ablated surfaces. The oxide layers feature a unique structure consisting of microscale (Ti,Zr,Hf)O_2 skeletons derived from $(Ti_{0.32}Zr_{0.32}Hf_{0.34})C_{micro}$, liquid SiO_2/(Zr,Hf)TiO_4 phases embedded with uniformly dispersed (Ti,Zr,Hf)O_2 nanoparticles derived from $(Ti_{0.32}Zr_{0.32}Hf_{0.34})C_{nano}$/SiC. The microscale (Ti,Zr,Hf)O_2 skeletons and (Ti,Zr,Hf)O_2 nanoparticles collectively protected the liquid phases from being blown away by air-plasma, similar to the wind resistance mechanism of multisized gravels in the Gobi Desert that stabilize mobile sands. Therefore, the synergistic effect of the micro-nano (Ti,Zr,Hf)C grains and their Gobi Desert-like structure improved the composites' ablation resistance. Overall, the development of micro-nano composites with high ablation resistance in this work provides critical insights into the microstructure and property optimization of UHTC-based composites and expands the design space for developing high-performance ablative materials.

Acknowledgements

The authors thank the National Natural Science Foundation of China (Nos. 52472082 and 52102085), the National Natural Science Fund for Excellent Young Scholars (Overseas), the Hunan Provincial Natural Science Foundation of China (No. 2024JJ6512), the National Key Laboratory of Science and Technology on High-strength Structural Materials, and the State Key Laboratory of Powder Metallurgy, Central South University, China (No. 621022335), for financial support.

Availability of data and materials

The data that support the findings of this study are available from the corresponding author upon reasonable request.

Competing interests

The authors have no competing interests to declare that are relevant to the content of this article.

Electronic Supplementary Material

Supplementary material is available in the online version of this article at https://doi.org/10.26599/JAC.2025.9221151.

References

[1] Rosenberg SD, Schoenman L. New generation of high-performance engines for space propulsion. *J Propuls Power* 1994, **10**: 40–46.

[2] Fu YQ, Zhang YL, Li T, *et al.* Effect of SiC on the anti-ablation resistance and flexural strength of (Hf–Ta–Zr)C–C/C composites. *J Eur Ceram Soc* 2024, **44**: 107–118.

[3] Li JC, Li T, Huang CJ, *et al.* The synergistic effect of multi-phase oxides on the ablation resistance of TaC-modified HfC–ZrC coatings for C/C composites. *Corros Sci* 2024, **228**: 111795.

[4] Lv JS, Li W, Li T, *et al.* Multicomponent (Hf–Zr–Ta)B_2 coatings for carbon/carbon composites and structural optimization enabling superior ablation resistance. *J Mater Sci Technol* 2025, **204**: 115–126.

[5] Ye ZM, Hu J, Zeng Y, *et al.* Probing solid-state diffusion and its synergistic role with preferential oxidation in enhancing the ablation performance of multiphase multicomponent carbide. *J Adv Ceram* 2025, **14**: 9221078.

[6] Hu JJ, Yang QK, Zhu SY, *et al.* Superhard bulk high-entropy carbides with enhanced toughness via metastable *in situ* particles. *Nat Commun* 2023, **14**: 5717.

[7] Peng Z, Cui YJ, Song JB, *et al.* The effect of nitrogen doping on the ablation resistance of zirconium carbide ceramics. *J Adv Ceram* 2025, **14**: 9221069.

[8] Cao ZN, Sun JL, Meng LT, *et al.* Progress in densification and toughening of high entropy carbide ceramics. *J Mater Sci Technol* 2023, **161**: 10–43.

[9] Ni DW, Cheng Y, Zhang JP, *et al.* Advances in ultra-high temperature ceramics, composites, and coatings. *J Adv Ceram* 2022, **11**: 550.

[10] Wang YC, Zhang BH, Zhang CY, *et al.* Ablation behaviour of (Hf–Ta–Zr–Nb)C high entropy carbide ceramic at temperatures above 2100 °C. *J Mater Sci Technol* 2022, **113**: 40–47.

[11] Yan ZH, Liu JX, Peng P, *et al.* Oxidation resistance of equimolar multicomponent transition metal carbide solid solution. *Adv Ceram* 2024, **45**: 541–557. (in Chinese)

[12] Guo HF, Moskovskikh D, Yudin S, *et al.* Annealing of a $(Hf_{0.2}Ta_{0.2}Ti_{0.2}Nb_{0.2}Zr_{0.2})C$ high-entropy ceramic up to 2100 °C: *In situ* removal of oxide impurities and microstructural modification. *Ceram Int* 2023, **49**: 37872–37880.

[13] Lu L, Du PC, Jiang TX, *et al.* Comparison of oxidation resistance of high-entropy $(Ti_{0.2}Zr_{0.2}Hf_{0.2}Ta_{0.2}Nb_{0.2})C$/SiC composites prepared by different methods at 1300–1600 °C. *J Eur Ceram Soc* 2025, **45**: 116885.

[14] Zhao T, Liu JX, Xu YX, *et al.* The effect of SiC on the laser ablation resistance of high-entropy diboride ceramics. *Adv Ceram* 2024, **45**: 417–433. (in Chinese)

[15] Wang YC, Yu D, Yin J, *et al.* Ablation behavior of (Hf–Ta–Zr–Nb–Ti)C high-entropy carbide and (Hf–Ta–Zr–Nb–Ti)C–*x*SiC composites. *J Am Ceram Soc* 2022, **105**: 6395–6406.

[16] Li F, Lu Y, Wang XG, *et al.* Liquid precursor-derived high-entropy carbide nanopowders. *Ceram Int* 2019, **45**: 22437–22441.

[17] Jiang YL, Ni DW, Chen BW, *et al.* Fabrication and optimization of 3D-C_f/HfC–SiC-based composites via sol-gel processing and reactive melt infiltration. *J Eur Ceram Soc* 2021, **41**: 1788–1794.

[18] Du B, Huang XM, Wang AZ, *et al.* Structure evolutions of the polymer derived medium-/ high-entropy metal carbides. *J Alloys Compd* 2023, **939**: 168737.

[19] Xie CY, Miao HM, Wan F, *et al.* Preparation of $(Ti_{0.2}Zr_{0.2}Hf_{0.2}Nb_{0.2}Ta_{0.2})C$ high-entropy ceramic nanopowders via liquid-phase precursor. *J Am Ceram Soc* 2024, **107**: 5105–5114.

[20] Fu YQ, Zhang YL, Yan H, *et al.* Microstructure and evolution of hafnium carbide whiskers via polymer-derived ceramics: A novel formation mechanism. *J Adv Ceram* 2023, **12**: 578–586.

[21] Ye ZM, Zeng Y, Xiong X, *et al.* New insight into the formation and oxygen barrier mechanism of carbonaceous oxide interlayer in a multicomponent carbide. *J Am Ceram Soc* 2020, **103**: 6978–6990.

[22] Zeng Y, Wang DN, Xiong X, *et al.* Ablation-resistant carbide $Zr_{0.8}Ti_{0.2}C_{0.74}B_{0.26}$ for oxidizing environments up to 3,000 °C. *Nat Commun* 2017, **8**: 15836.

[23] Zhang J, Zhang YL, Chen RC, *et al.* Effect of microstructure on the ablation behavior and mechanical properties of CVD-HfC coating. *Corros Sci* 2021, **192**: 109815.

[24] Ren JC, Feng ER, Zhang YL, *et al.* Microstructure and anti-ablation performance of HfC–TaC and HfC–ZrC coatings synthesized by CVD on C/C composites. *Ceram Int* 2020, **46**: 10147–10158.

[25] Cai FY, Ni DW, Chen BW, *et al.* Fabrication and properties of C_f/$(Ti_{0.2}Zr_{0.2}Hf_{0.2}Nb_{0.2}Ta_{0.2})C$–SiC high-entropy ceramic matrix composites via precursor infiltration and pyrolysis. *J Eur Ceram Soc* 2021, **41**: 5863–5871.

[26] Chen MW, Zhao YL, Qiu HP, *et al.* Ablative behavior and mechanism of SiC_f/SiBCZr composites prepared by PIP process. *J Adv Ceram* 2024, **13**: 124–134.

[27] Lyu Y, Han ZH, Zhao GD, *et al.* Efficient fabrication of light C_f/SiHfBOC composites with excellent thermal shock resistance and ultra-high-temperature ablation up to 1800 °C. *J Adv Ceram* 2023, **12**: 2062–2074.
[28] Ionescu E, Kleebe HJ, Riedel R. Silicon-containing polymer-derived ceramic nanocomposites (PDC–NCs): Preparative approaches and properties. *Chem Soc Rev* 2012, **41**: 5032.
[29] Lu Y, Sun YN, Zhang TZ, *et al.* Polymer-derived Ta_4HfC_5 nanoscale ultrahigh-temperature ceramics: Synthesis, microstructure and properties. *J Eur Ceram Soc* 2019, **39**: 205–211.
[30] Yang HT, Klemm S, Müller J, *et al.* Synthesis of high-entropy carbides from multi-metal polymer precursors. *J Eur Ceram Soc* 2023, **43**: 4233–4243.
[31] Wen QB, Luan XG, Wang L, *et al.* Laser ablation behavior of SiHfC-based ceramics prepared from a single-source precursor: Effects of Hf-incorporation into SiC. *J Eur Ceram Soc* 2019, **39**: 2018–2027.
[32] Wen QB, Riedel R, Ionescu E. Significant improvement of the short-term high-temperature oxidation resistance of dense monolithic HfC/SiC ceramic nanocomposites upon incorporation of Ta. *Corros Sci* 2018, **145**: 191–198.
[33] Wen QB, Riedel R, Ionescu E. Solid-solution effects on the high-temperature oxidation behavior of polymer-derived (Hf,Ta)C/SiC and (Hf,Ti)C/SiC ceramic nanocomposites. *Adv Eng Mater* 2019, **21**: 1800879.
[34] Lu L, Wen QB, Hu JR, *et al.* Single-source-precursor synthesis and air-plasma ablation behavior of (Ti,Zr,Hf)C/SiC ceramic nanocomposites at 2200 °C. *J Adv Ceram* 2024, **13**: 1043–1059.
[35] Zhang XX, Yang X, Luo X, *et al.* Formation mechanism of (Ti,Zr,Hf)C medium-entropy carbide derived from polymer precursors and its modification on the ablative mechanism of C/C-SiC composites. *Corros Sci* 2024, **230**: 111935.
[36] Zhang KC, Qu JJ, Zu RP, *et al.* Characteristics of wind-blown sand on Gobi/mobile sand surface. *Environ Geol* 2008, **54**: 411–416.
[37] Denton AR, Ashcroft NW. Vegard's law. *Phys Rev A* 1991, **43**: 3161–3164.
[38] Wang LW, Wei BX, Wang D, *et al.* Novel α/β SiC–$(Ti,Nb)B_2$ toughened (Ti,Nb)C-based composites with enhanced mechanical properties fabricated by *in situ* reactions sintering at low temperature. *Ceram Int* 2024, **50**: 46211–46226.
[39] Ma H-B, Xue J-X, Zhai J-H, *et al.* Pressureless joining of silicon carbide using Ti_3SiC_2 MAX phase at 1500°C. *Ceram Int* 2020, **46**: 14269–14272.
[40] Yan XL, Constantin L, Lu YF, *et al.* $(Hf_{0.2}Zr_{0.2}Ta_{0.2}Nb_{0.2}Ti_{0.2})C$ high-entropy ceramics with low thermal conductivity. *J Am Ceram Soc* 2018, **101**: 4486–4491.
[41] Wang YJ, Li HJ, Fu QG, *et al.* Ablative property of HfC-based multilayer coating for C/C composites under oxy-acetylene torch. *Appl Surf Sci* 2011, **257**: 4760–4763.
[42] Guo WJ, Hu J, Ye YC, *et al.* Ablation behavior of (TiZrHfNbTa)C high-entropy ceramics with the addition of SiC secondary under an oxyacetylene flame. *Ceram Int* 2022, **48**: 12790–12799.
[43] Zheng W, He XB, Wu M, *et al.* Thermal expansion coefficient of Diamond/SiC composites prepared by silicon vapor infiltration in vacuum. *Vacuum* 2019, **159**: 507–515.
[44] Vegard L. Die konstitution der mischkristalle und die raumfüllung der atome. *Z Physik* 1921, **5**: 17–26. (in German)
[45] Castle E, Csanádi T, Grasso S, *et al.* Processing and properties of high-entropy ultra-high temperature carbides. *Sci Rep* 2018, **8**: 8609.
[46] Li JC, Lu FY, Li T, *et al.* The interface interaction within multi-phase oxides on the ablation behavior of the $(Hf_{0.25}Zr_{0.25}Ti_{0.5})C$-coated C/C composites. *Surf Coat Tech* 2024, **493**: 131293.
[47] Peng P, Liu JX, Xin XT, *et al.* Dual-phase medium-entropy diboride–carbide ceramics with metal element exchange during sintering. *J Adv Ceram* 2025, **14**: 9221007.
[48] Wen QB, Qu FM, Yu ZJ, *et al.* Si-based polymer-derived ceramics for energy conversion and storage. *J Adv Ceram* 2022, **11**: 197–246.
[49] Peng Z, Sun W, Xiong X, *et al.* Novel refractory high-entropy ceramics: Transition metal carbonitrides with superior ablation resistance. *Corros Sci* 2021, **184**: 109359.
[50] Zhang J, Jiang JM, Song Q, *et al.* Ultra-high temperature ablation property of $Ta_{0.5}Hf_{0.5}C$ ternary ceramic under plasma flame. *Ceram Int* 2021, **47**: 28050–28054.
[51] Nieto A, Kumar A, Lahiri D, *et al.* Oxidation behavior of graphene nanoplatelet reinforced tantalum carbide composites in high temperature plasma flow. *Carbon* 2014, **67**: 398–408.
[52] Peng Z, Sun W, Xiong X, *et al.* Thermoablative behaviors of designable hafnium carbonitride integrated with lattice of tungsten upon 3273 K. *Corros Sci* 2021, **188**: 109504.
[53] Li JC, Zhang YL, Zhao YX, *et al.* A novel $(Hf_{1/3}Zr_{1/3}Ti_{1/3})C$ medium-entropy carbide coating with excellent long-life ablation resistance applied above 2100 °C. *Compos Part B Eng* 2023, **251**: 110467.
[54] Backman L, Gild J, Luo J, *et al.* Part I: Theoretical predictions of preferential oxidation in refractory high entropy materials. *Acta Mater* 2020, **197**: 20–27.
[55] Hu Y, Ni DW, Chen BW, *et al.* C_f/(CrZrHfNbTa)C–SiC high-entropy ceramic matrix composites for potential multi-functional applications. *J Mater Sci Technol* 2024, **182**: 132–140.
[56] Ye ZM, Zeng Y, Xiong X, *et al.* Elucidating the role of preferential oxidation during ablation: Insights on the design and optimization of multicomponent ultra-high temperature ceramics. *J Adv Ceram* 2022, **11**: 1956–1975.
[57] Chen XW, Feng Q, Zhou HJ, *et al.* Ablation behavior of three-dimensional C_f/SiC–ZrC–ZrB_2 composites prepared by a joint process of sol-gel and reactive melt infiltration. *Corros Sci* 2018, **134**: 49–56.
[58] Cai FY, Ni DW, Bao WC, *et al.* Ablation behavior and mechanisms of C_f/$(Ti_{0.2}Zr_{0.2}Hf_{0.2}Nb_{0.2}Ta_{0.2})C$–SiC high-entropy ceramic matrix composites. *Compos Part B Eng* 2022, **243**: 110177.
[59] Jing X, Zhao W, Lan L. The effect of particle size on electric conducting percolation threshold in polymer/conducting particle composites. *J Mater Sci Lett* 2000, **19**: 377–379.
[60] Zou J, Rubio V, Binner J. Thermoablative resistance of ZrB_2–SiC–WC ceramics at 2400 °C. *Acta Mater* 2017, **133**: 293–302.